May 2020

Power Electronic Architecture for Multi-Vehicle Extreme Fast Charging Stations

Nicholas Hoeft
University of Wisconsin-Milwaukee

POWER ELECTRONIC ARCHITECTURE FOR MULTI-VEHICLE EXTREME FAST CHARGING STATIONS

by

Nicholas Hoeft

A Thesis Submitted in
Partial Fulfillment of the
Requirements for the Degree of

Master of Science
in Engineering

at

The University of Wisconsin-Milwaukee

May 2020

ABSTRACT

POWER ELECTRONIC ARCHITECTURE FOR MULTI-VEHICLE EXTREME FAST CHARGING STATIONS

by

Nicholas Hoeft

The University of Wisconsin-Milwaukee, 2020
Under the Supervision of Professor Robert Cuzner

Electric vehicles (EV) are quickly gaining popularity but limited driving range and a lack of fast charging infrastructure are preventing widespread use when compared with gas powered vehicles. This gave rise to the concept of multi-vehicle extreme fast charging (XFC) stations. Extreme fast charging imposes challenges in the forms of power delivery, battery management, and energy dispatch. The extreme load demand must be handled in such a way that users may receive a timely charge with minimal impacts on the electric grid. Power electronics are implemented to address these challenges with highly power dense and efficient solutions. This work explores a power electronic architecture as one such solution. The system consists of three parts: a cascaded H-bridge (CHB) active rectifier that interfaces to a medium voltage (MV) grid, a dual active bridge (DAB) based solid state transformer (SST) that provides isolation and forms a low voltage DC (LVDC) bus, and full bridge DC-DC converters configured as partial power converters (PPC) that interface with the vehicle battery.

DEDICATION

First, I would like to thank my professor, Dr. Robert Cuzner, for giving me the opportunity to join his research team, inspiring me to continue my education, and encouraging me along the way. I would also like to thank my family for their loving support. Finally, I would like to thank everyone from the roofless lab who I have shared many laughs and ideas with over the years.

TABLE OF CONTENTS

LIST OF FIGURES

LIST OF TABLES

GLOSSARY OF ACRONYMS AND SYMBOLS

BEV = Battery Electric Vehicle

BMS = Battery Management System

CC-CV = Constant Current Constant Voltage

CHB = Cascaded H-bridge

CPS-SPWM = Carrier Phase Shifted Sinusoidal PWM

DAB = Dual Active Bridge

EV = Electric Vehicle

EVSE = Electric Vehicle Supply Equipment

ICEV = Internal Combustion Engine Vehicle

ISOP = Input-Series Output-Parallel

LFT = Line Frequency Transformer

LVac = Low Voltage Alternating Current

LVDC = Low Voltage Direct Current

MSCCC = Multi-Stage Constant Current Charging

MVac = Medium Voltage Alternating Current

MVDC = Medium Voltage Direct Current

PLL = Phase-locked Loop

PPC = Partial Power Converter

SAB = Single Active Bridge

SoC = State of Charge

SST = Solid-state Transformer

V2G = Vehicle to Grid

VSC = Voltage Source Converter

XFC = Extreme Fast Charging

ACKNOWLEDGEMENTS

This material is based upon work supported by the National Science Foundation under Grant No. 1747757. Any opinions, findings, and conclusions or recommendations expressed in this material are those of the author(s) and do not necessarily reflect the views of the National Science Foundation.

CHAPTER 1
INTRODUCTION AND BACKGROUND

The passenger electric vehicle was invented in the late 19th century and was the preferred choice of vehicle at the time. Electric vehicles brought with them many attractive qualities when compared with internal combustion engine vehicles (ICEVs). Drivers found that with electric propulsion, their vehicles were easier to use and ran cleaner and quieter than those powered by gasoline. However, EVs suffered from a short driving range and many people did not have access to adequate electricity for charging. With the advent of the mass-produced Model T, people had gained access to a much more affordable option that offered a long range and easily accessible fuel source. By the 1920s, ICEVs had flooded the market, and EVs were effectively phased out by the end of 1935.

In recent efforts to combat climate change due to greenhouse gases, specifically CO_2 gas emissions, technologies are being developed to make the transition from fossil fuels to more sustainable technologies. In the U.S., the main contributors of CO_2 emissions are coming from the energy sector and the transportation sector, each contributing 33% and 34% of total emissions, respectively [1]. Focusing on the transportation sector, there has been a significant push for the use and development of electric vehicles. Currently, EVs only make up an estimated 0.5% of vehicles on the road today. However, with advancements in battery technology and competitive markets, EV sales are expected to grow exponentially in the coming years [2]. Progress has been slow-going as limited driving range and lack of charging infrastructure has left current and future electric vehicle owners with range anxiety [3].

Internal combustion engine vehicles have been used for decades and thus the gas station infrastructure is vast and well established. To compete with ICEVs, a paradigm shift is required in the way we charge [4],[5]. Following the gas station model, the concept of extreme fast charging (XFC) stations was realized. Typically, battery electric vehicles are charged at home and overnight. This charging process uses chargers which are relatively low power and take many hours for a full

charge. These chargers are insufficient in a long-range scenario where people may need to charge their battery along the way. In an extreme fast charging scenario, a vehicle may receive a full 20%-80% charge in under 10 minutes. This allows the end user to quickly charge their vehicle and continue their trip with little to no interruption akin to fueling up an ICEV at a gas station. With XFC stations, EV use can expand to new markets currently restricted by existing charging infrastructure. This includes but is not limited to home renters who may not have access to regular charging, rideshare workers who continuously drive throughout the day, and anyone who needs to drive long distances. In addition, an XFC station development helps to pave the way into charging medium and heavy-duty vehicle fleets [6]. To achieve this, however, there are many challenges that need to be overcome [7], [8]. These challenges manifest in many forms such as battery management, power throughput at the battery interface, energy delivery, and potential impacts to the electric grid.

This thesis will cover the following topics:

Chapter 2 Discusses the current trends and requirements for XFC systems.

Chapter 3 Discusses the development of the EV battery interfacing converter including modeling and control.

Chapter 4 Discusses the development of the MVAC active front end converter and solid state transformer including modeling and control.

Chapter 5 Verifies the operation of the XFC system through simulation and discusses the results.

Chapter 6 Concludes the thesis and makes recommendations for future work.

CHAPTER 2
CURRENT TRENDS AND SYSTEM REQUIREMENTS

2.1 Evolution of EV Charging

Electric vehicle battery chargers have an integral role in the widespread use of EVs, and the way people charge their cars is constantly changing [9],[10]. Currently there are three main types of battery chargers which are categorized based on voltage and power levels, charging time, and location. The location of the charger refers to where it is located relative to the vehicle; that is, inside (on-board) or outside (off-board) of the EV. Table 2.1 provides a summary of the main differences between charging levels.

2.1.1 Level 1 Charging

Level 1 battery charging is designed for residential use, requiring only a 120V single-phase connection. This is an on-board charger where AC voltage is plugged directly into the vehicle and converted to the appropriate DC voltage for charging inside of the vehicle. Low capital cost and ease of use make this a very popular option. Users are able to plug in their vehicles at home to charge overnight. However, the low power throughput of level 1 charging becomes a bottleneck on charging times, taking many hours to charge a BEV.

2.1.2 Level 2 Charging

Level 2 battery charging is largely the same as level 1 with about an order of magnitude increase in power level. Rather than the single-phase connection of level 1, level 2 charging uses a three-phase connection to utilize the 208V/240V connections found in the U.S. Again, the charging is done on-board for this level. Because these chargers require an available three phase connection as well as having a higher capital cost, they are less commonly found at the residential level. Many

level 2 chargers can be found at a commercial level. Public charging connections, commonly available outside of businesses, have a tapped connection with the option of level 2 or level 1 charging at a reduced rate.

2.1.3 Level 3 Charging

Level 3 charging is the first major change in charging infrastructure. Level 3 charging uses off-board chargers and is oftentimes referred to as DC-fast charging. By placing the charging converter outside of the vehicle, off-board chargers are no longer restricted to the sizing requirements that on-board chargers adhere to. This allows for a higher power conversion that supplies DC current directly to the battery pack. Comparatively, these chargers are large, expensive, and intended for commercial use. Level 3 charging is the first look into a budding charging infrastructure that follows the gas station model. However, not all EV models are equipped to handle the high power output of level 3 charging. Tesla reports peak charging rates up to 250kW with their V3 super-chargers, but only their high-end vehicle models are capable of receiving this amount of power [11]. With level 3 charging, full charge times of BEVs can be reduced to approximately 15 to 30 minutes, depending on energy capacity.

2.1.4 Extreme Fast Charging

Extreme fast charging can be used to describe the next generation of fast chargers. With the proliferation of 1.2kV voltage class devices, the next generation of EVs are tending towards 800V battery packs [12]. This is further evidenced with the recently released Porsche Taycan which already uses the new 800V battery architecture [13]. To compete, automakers such as Audi, Ford, and General Motors are releasing plans for their own 800V battery vehicles in the near future [14][15][16]. The increased voltage level allows for a further increase in power throughput, lending itself suitable for XFC application. To achieve full charging times of 10 minutes and under, XFC chargers would require power outputs in excess of 350kW. For a commercial application, 350kW chargers can potentially increase customer throughput by about 70% when compared to the related

400V systems [12]. Average trips of five minutes can then be achieved, akin to a regular gas station visit.

Table 2.1: EV Charging Levels

Charging Level	Voltage Level	Power Level	Charger Location
Level 1	120V$_{ac}$	1-2kW	On-board
Level 2	240V$_{ac}$	4-20kW	On-board
Level 3 (DC-fast)	480V$_{dc}$	50-250kW	Off-board
XFC	800-1kV$_{dc}$	350kW+	Off-board

2.2 Charging Infrastructure

2.2.1 Charging at Home

The most common method of EV charging is done at home using level 1 or level 2 charging, shown in Fig 2.1. Level 1 charging is the ultimate convenience charger as a vehicle owner can charge using virtually any electrical outlet available at home. As mentioned, the charging capability of Level 1 is quite restrictive when relied upon as a primary charging source, taking more than 12 hours for a full charge. Another at-home option is to purchase electric vehicle supply equipment (EVSE) approved for level 2 charging in accordance with SAE J1772. This can be installed in a permanent location, such as a garage, using a capable circuit. As highlighted in Fig 2.1, conventional protection equipment is sufficient. For level 2 charging, ground fault protection is required.

2.2.2 Charging at Commercial Locations

To extend the range of EV batteries outside of the home, many businesses have publicly available charging stations. They can be found outside of shopping centers, outside of the workplace, or in public parking lots. As shown in Fig 2.2, highlighted in blue, a nearby distribution transformer with sufficient ratings can be used to interface multiple chargers to the grid. Oftentimes this public

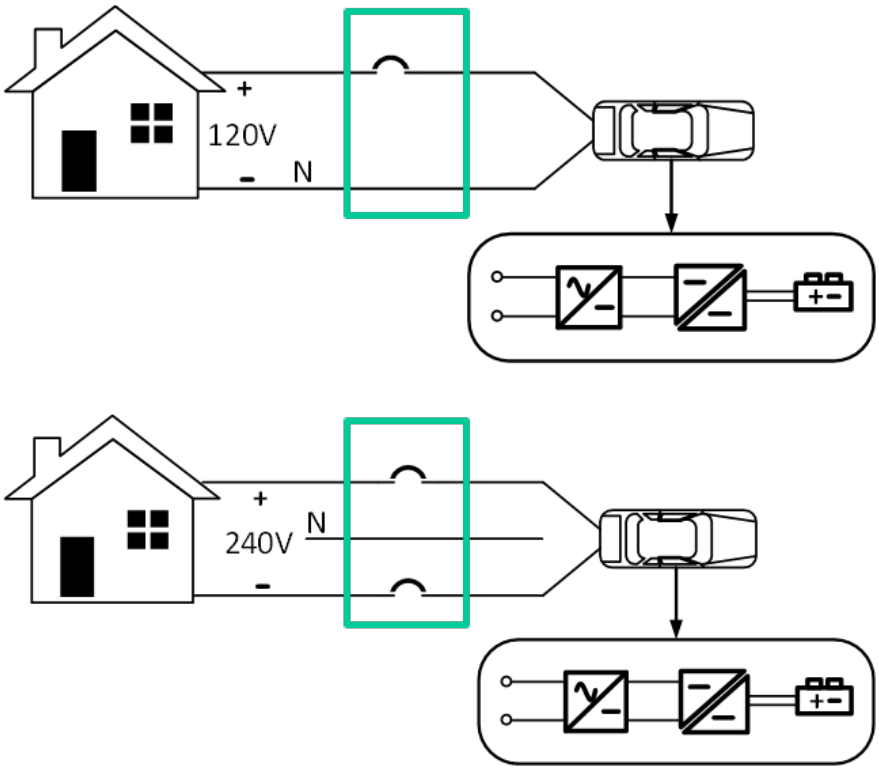

Figure 2.1: At Home Charging Interface

access charging is a level 1 ”courtesy” charge with the option to purchase level 2 charging at a small cost. Public charging is conducted with the same EVSE and safety standards as residential charging. The SAE J1772 coupling protocol lends itself well to public charging as it is compatible with virtually every EV. Operating at low power, these publicly available chargers can only service a couple vehicles in a given day.

2.2.3 Multi-Vehicle Charging Stations

To service EV users on the go, some companies have built dedicated charging stations that currently offer level 3 DC-fast charging for a fee. The ideal location for these stations are along highway systems or urban areas with heavy traffic. With multiple charging ports, these systems can service many vehicles a day. An example station can be seen in Fig 2.3. It consists of an AC-DC rectifier that interfaces with the grid to form a DC bus. Multiple dedicated chargers can then be connected in parallel to service multiple vehicles at one time. Because these systems

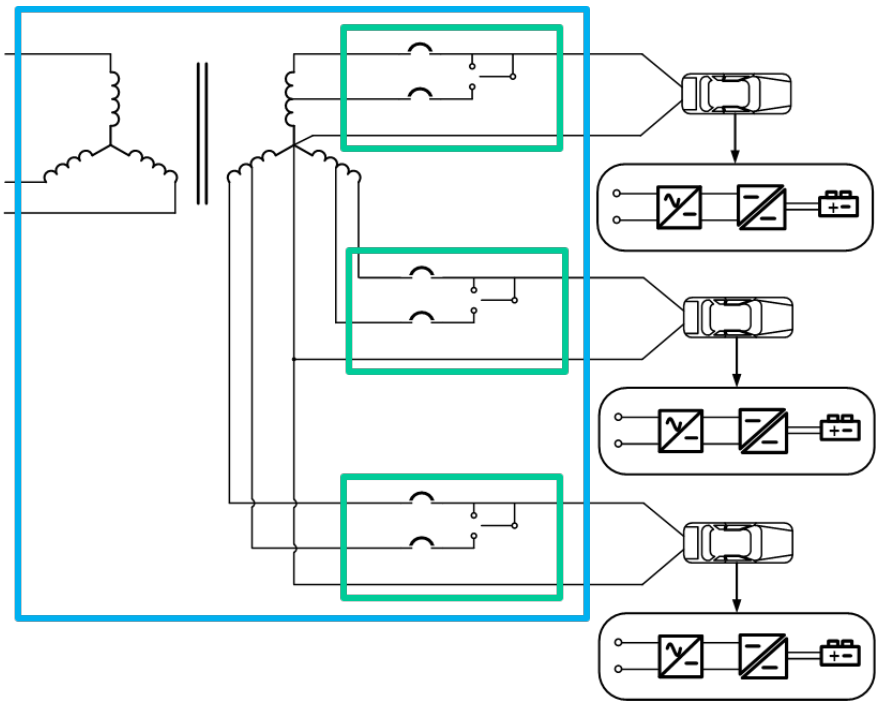

Figure 2.2: Public Charging Interface

use dedicated off-board chargers, many more safety standards and specifications must be met in accordance with IEEE Std. 2030.1.1 [17]. This includes, but is not limited to, isolation from the grid, a communication channel between the battery and charger, and isolating contactors capable of breaking charge current. Additionally, existing fast charger coupling protocols are region specific and suffer from incompatibilities between vehicle make and model. Table 2.2 summarizes the ratings of each protocol and their respective regions. Applying this system concept to XFC stations would simply be an expansion upon this infrastructure with increased capabilities. As there are not yet specific standards put in place for XFC levels of charging, the current IEEE 2030.1.1 standards should be considered.

Table 2.2: EV Charger Coupling Protocols

Protocol	Max Voltage	Max Current	Region
CCS (Type 1)	1000V	350A	United States
CCS (Type 2)	1000V	350A	Europe
CHAdeMO 2.0	1000V	350A	Japan
GB/T	1000V	400A	China

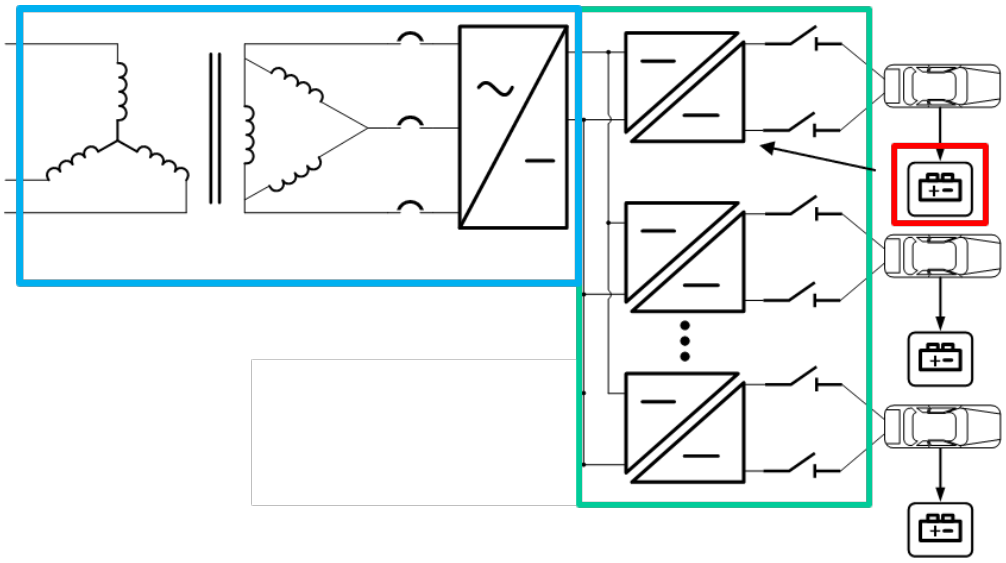

Figure 2.3: Example Multi-Vehicle Charging Station

2.3 EV Battery Considerations

2.3.1 Battery Type

The electric vehicle battery type and battery management play a key role in the viability of XFC stations. To enable XFC, a battery pack must be of suitable type to handle high power input while maintaining its longevity. Many different battery types have been considered and used in BEVs, each having their own advantages and disadvantages [18]. In previous years, the common choice of battery chemistry was lead acid. Lead acid has a relatively high power density and is very inexpensive to manufacture. However, their major disadvantage is they have low energy density. Since their chemistry is composed of lead, they are also considered to be environmentally unfriendly to produce. Seeking other battery solutions, various other chemistries such as nickel-cadmium, nickel-metal-hydride, Li-ion batteries, among others, have been explored [18]. Li-ion batteries have high power density, high energy density, high cell voltage, and low self-discharge making them an ideal candidate for BEVs, and subsequently, XFC application [19]. The primary hindrance to widespread use of Li-ion batteries has been their high cost. In recent years, economies of scale and a competitive market have dramatically decreased the price of Li-ion batteries and has

made Li-ion the go-to choice for BEV manufacturers [20].

2.3.2 Battery Management

In order to maintain the longevity of a battery, a battery management system (BMS) must be implemented. The BMS should not only exist inside of the EV for state of charge (SoC) monitoring, but there must also exist a BMS at the XFC charger [17]. Li-ion batteries are particularly susceptible to overcharging and undercharging and doing so will greatly diminish the life cycle of the battery [19]. Thermal management is another key aspect of a BMS [21]. Rapid temperature rises caused by the power throughput of XFC can be detrimental to the health of a battery, and in the case of Li-ion batteries, it can cause a chemical reaction known as lithium plating [22]. The study conducted in [22] provides a charging technique which brings a battery to temperature before beginning the XFC process that prevents this phenomenon from occurring. By raising the EV battery to temperatures of 60°C before charging and subsequently cooling the battery during discharge, the life of the battery is greatly extended. This simple technique is a major advancement that further pushes the viability of extreme fast charging towards being an acceptable charging routine.

2.4 XFC Battery Interface

2.4.1 Coupling Protocol

The existing coupling protocols, outlined in Table 2.2, claim power ratings of up to 350kW. To reach those power ratings, however, the charger would have to operate at its maximum ratings of 1000V and 350A (400A for China's GB/T). To achieve charging powers of 350kW and up for an 800V battery architecture, current ratings would have to exceed 400A. Recent developments have been made by the ChaoJi group to create a protocol capable of XFC [23]. The CHAdeMO 3.0 is expected to enable charging powers of over 500kW with a maximum current rating of 600A. Additionally, it offers backwards compatibility with existing fast charging protocols CHAdeMO 2.0 and GB/T, with possible CCS compatibility. With coupling incompatibilities solved, true multi-vehicle XFC stations become viable.

2.4.2 Bidirectional Chargers

There have been many studies on bidirectional chargers which can use a fleet of vehicle batteries to support the grid, referred to as vehicle-to-grid (V2G) [24],[25]. If there exists a sufficiently large charging station, the combined capacity of the BEVs may be used as a battery energy storage system (BESS). If this is the case, then the vehicle fleet may provide grid support much like a normal BESS by providing active power and/or reactive power compensation. While these technologies offer a more flexible decision making for charging, the control strategies become very complex and difficult to achieve. Additional challenges come in the form of advanced metering requirements, increased converter cost and frequent cycling which can degrade the health of the battery. The use of V2G can be applied to level 1 and level 2 chargers but typically are not considered at level 3 charging. Applying V2G to XFC applications would only exacerbate these issues further, therefore it is not considered in this study.

2.4.3 Unidirectional Chargers

With unidirectional charging, the controls become relatively simple and the number of active devices can be reduced. The battery charging converter should also be chosen such that it can process XFC levels of power with relatively high efficiency. Implementing such a converter in a single conversion stage can keep combined costs low and become more attractive to potential XFC station owners.

2.5 XFC Grid Interface

Deploying a charging station with multiple XFC level chargers can quickly ramp up in power demand. With just four XFC chargers that have a potential charging rate of 350kW, the system must be capable of delivering at least 1.4 MW of power. Furthermore, the load profile can change unexpectedly throughout the day. If handled improperly, this can cause strain on the local distribution system, especially during on-peak hours when these stations are more likely to be used [26].

Additionally, IEEE Std. 2030.1.1 requires the input power supply to have a power factor no less than 0.95 and AC-DC conversion efficiency of at least 90%. To be successful, the grid interface must be highly controllable and operate efficiently over a wide range of loads.

2.6 Proposed XFC Architecture

The proposed system architecture is given in Fig 2.4. The grid interface consists of three parts: a solid state transformer, an energy buffer stage, and a bus balancing stage. The SST is composed of a combined cascaded H-bridge and dual active bridge. It fulfills the isolation requirement from the grid in a highly efficient and controllable manner. The energy buffer stage splits the output of the SST to form a bipolar LVDC bus. This improves the operation of the SST by reducing the voltage conversion it has to perform. Furthermore, the energy buffer serves the purpose of mitigating transients while supporting the LVDC bus. The bus balancing stage maximizes controllability of the system by providing a means to adjust the inputs of the battery interfacing converters. With the isolation requirement satisfied, a highly efficient, non-isolated DC-DC converter is use to interface with the battery.

This work aims to provide an in-depth analysis of the system's functionality and performance as a multi-vehicle charging system. For this purpose, the system provided in Fig 2.5 is formed and analyzed. The studied system architecture consists of the SST as the grid interface with the battery interfacing converters paralleled on a single LVDC bus.

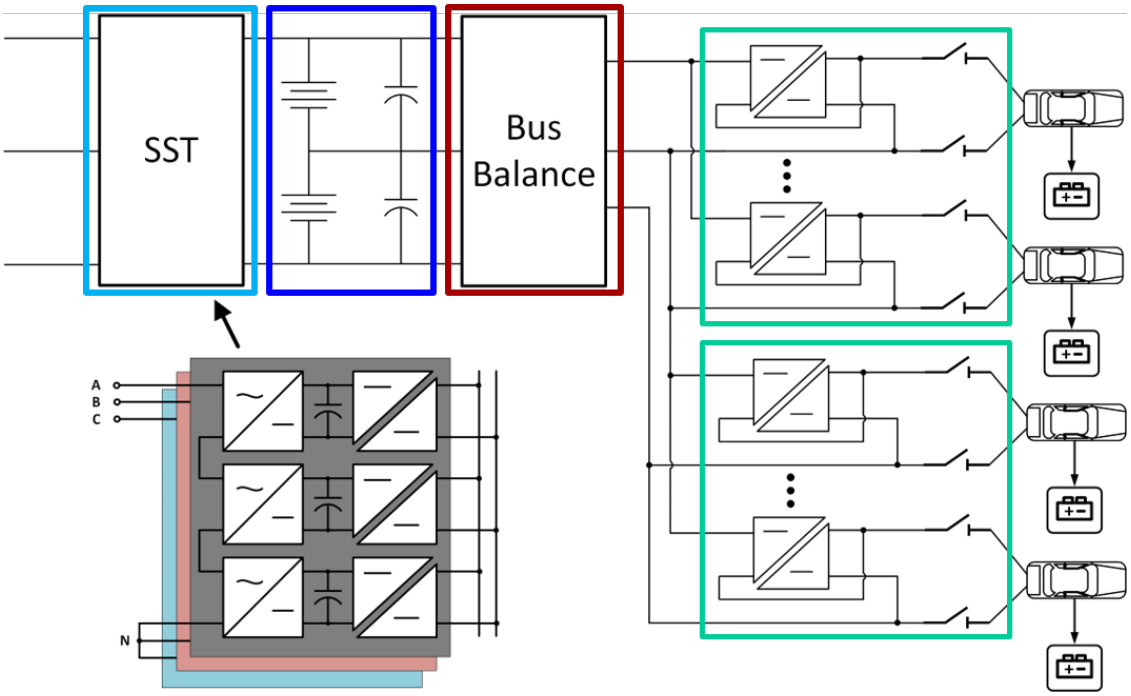

Figure 2.4: Proposed Multi-Vehicle XFC Station Architecture

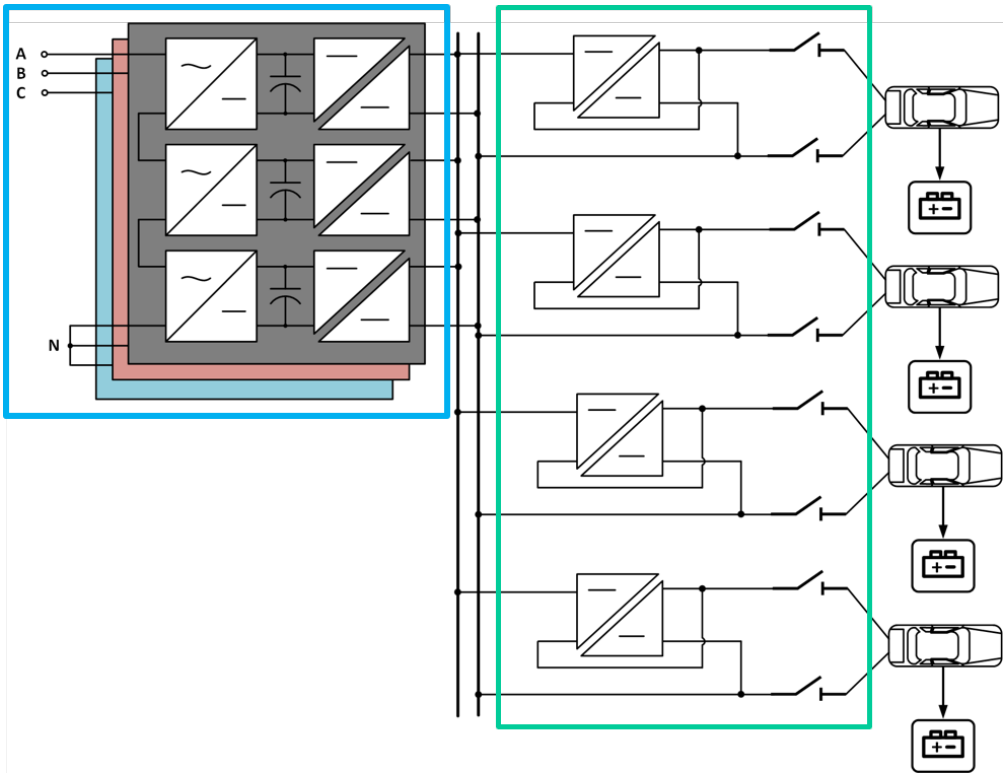

Figure 2.5: Studied Multi-Vehicle XFC Station Architecture

CHAPTER 3
ELECTRIC VEHICLE BATTERY INTERFACE

To service BEVs at the XFC level, the battery interfacing power converter must be capable of significant power delivery. Additionally, a control scheme must be implemented that can take the EV battery's state of charge (SoC) into consideration, so as not to overcharge and potentially degrade the battery.

3.1 Partial Power Converter Configuration

One battery interface converter that is gaining popularity is the partial power converter (PPC) [27][28][29]. This converter type uses an isolated DC-DC converter topology, such as a single active bridge (SAB) or dual active bridge (DAB), which is then configured as a partial power converter. The partial power configuration, shown in Fig 3.1, makes a direct connection from the input to the output of the converter. This places the devices solely on the active portion of the converter, processing only a fraction of the power, thus improving overall efficiency. Additionally, the devices can be partially rated, improving cost effectiveness and increasing power density. However, the partial power configuration does come with limitations. The direct connection from input to output causes a lack of source to load isolation, the input to output voltage gain is limited, and the converter topology requires a transformer. The use of a DAB converter topology allows for bidirectional operation; however, the SAB is chosen for this unidirectional application.

3.2 PPC Operation

To better understand the PPC, the basic operation stages are discussed in this section. The PPC consists of two main operating stages: the active switch stage and the freewheeling stage. During the active switching stage, shown in Fig 3.2, both switch legs of the controlled H-bridge

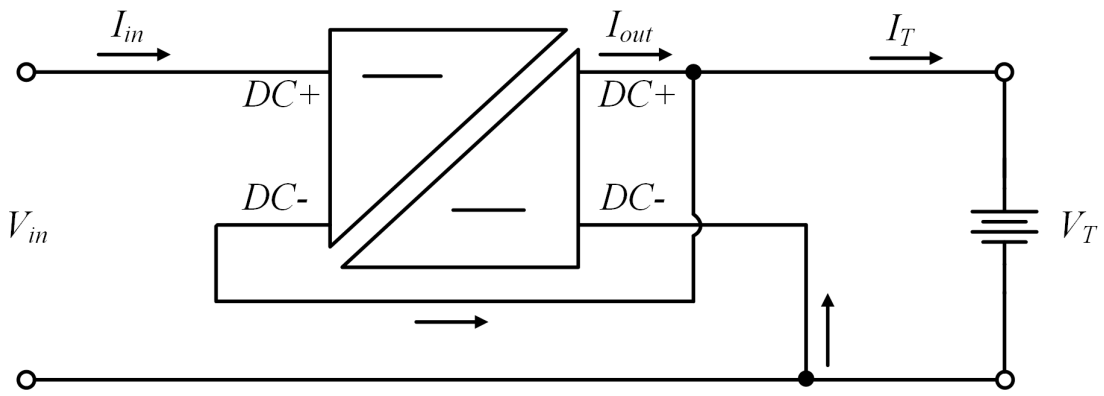

Figure 3.1: Partial Power Converter Configuration

and clamping circuit are turned on. The switch legs pass the majority of current which gets fed forward to the output while exciting the transformer. The step-up transformer then forward biases the diode bridge which creates a bypass circuit at the output to supply the remaining current. The clamping circuit is used to hold a DC voltage across the active switching devices as well as mitigate overvoltages and oscillations. Fig 3.3 shows the freewheeling stage that starts by turning off all switches. The diode bridge continues commutating current from the secondary of the transformer until the diodes become reverse biased and turn off. The next active stage begins with the same operation as shown in Fig 3.2 but with the opposite pair of switch legs. The switching pattern then continues as described, alternating between switch legs during the active switching stage.

3.3 PPC Modeling and Limitations

As mentioned, the PPC has limitations in terms of the input to output voltage range. Assuming lossless conditions, the voltage transformation ratio, G_v, exhibits the following relationship.

$$G_v = \frac{2dn}{2dn + 1} \tag{3.1}$$

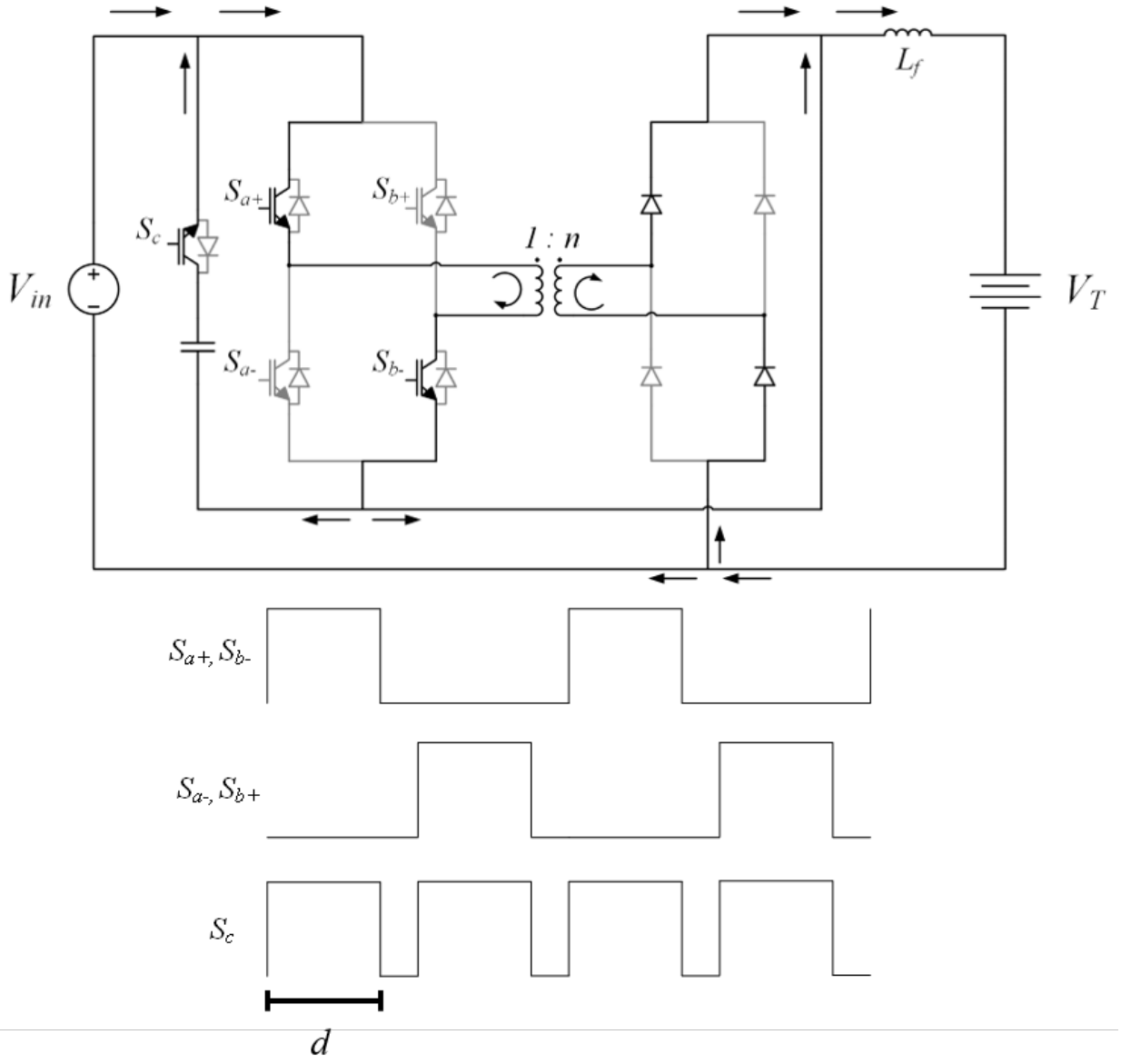

Figure 3.2: PPC Active Switch Stage

The duty cycle, d, is limited to $0 \leq d \leq 0.5$, therefore the transformer turns ratio, n, determines the maximum voltage transformation given by

$$G_{v_{max}} = \frac{n}{n+1} \quad for \quad d = 0.5 \tag{3.2}$$

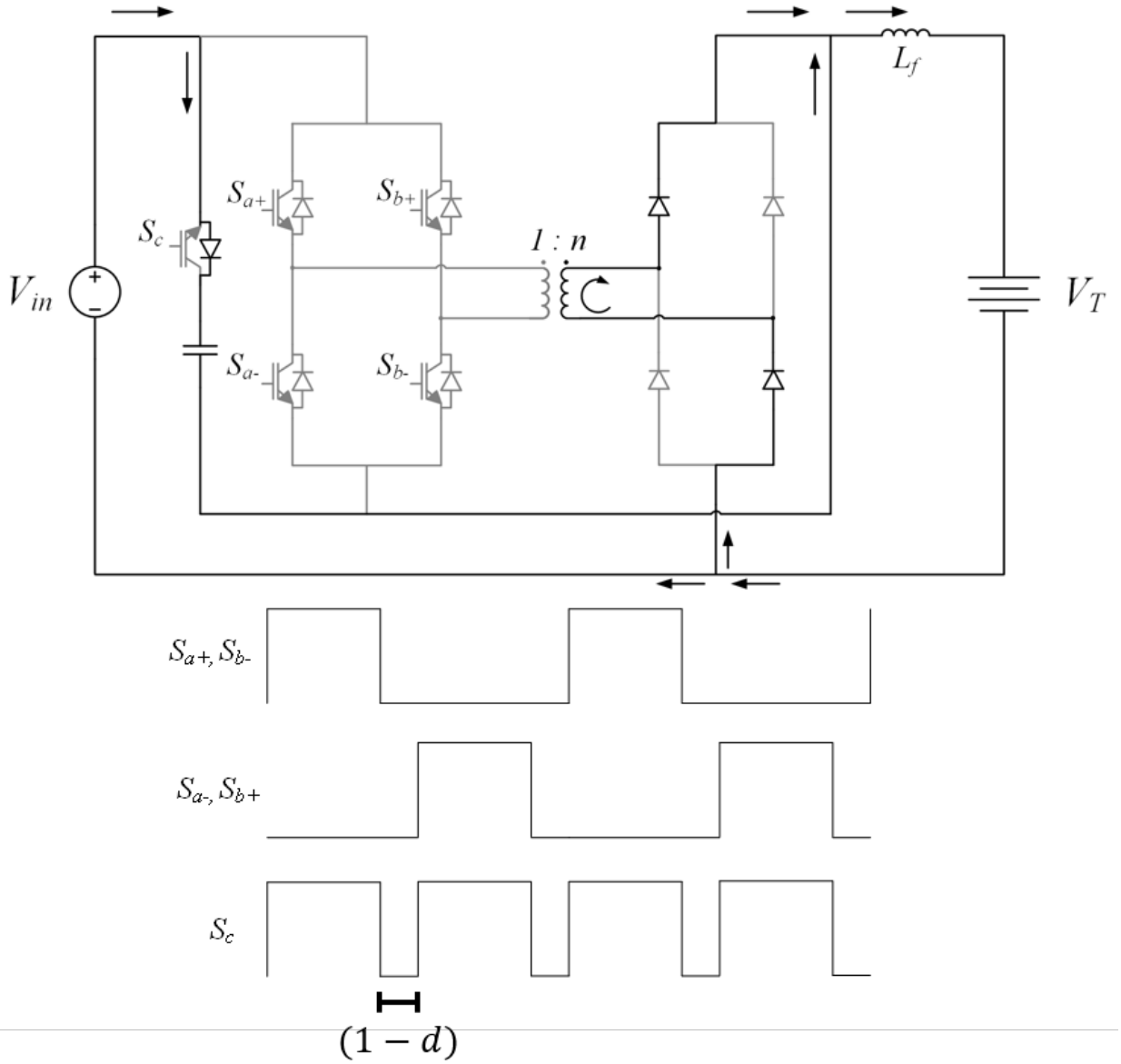

Figure 3.3: PPC Freewheeling Stage

Fig 3.4 plots G_v as the duty cycle varies for different transformer turns ratios. The partial power ratio which represents the percentage of output power that the converter processes is given by

$$PPR = \frac{V_i - V_o}{V_i} \tag{3.3}$$

therefore

$$PPR = 1 - G_v \tag{3.4}$$

From (3.4) it becomes apparent that as G_v approaches 1, efficiency, power density, and cost effectiveness increase.

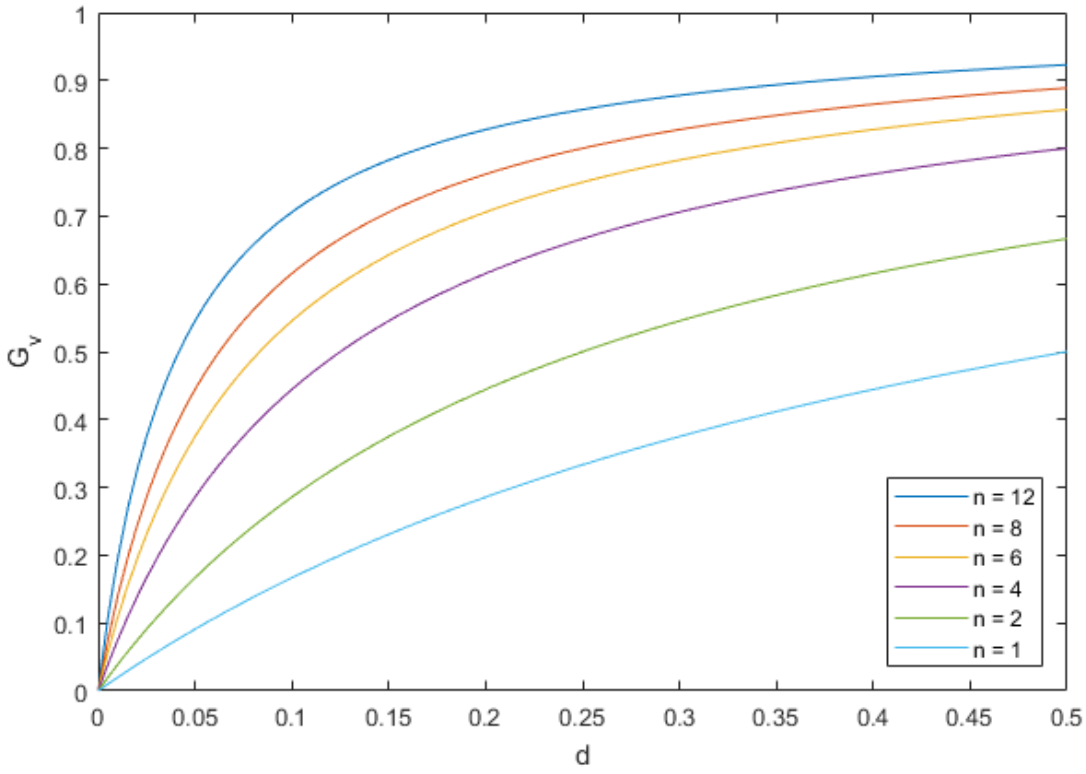

Figure 3.4: Relationship Between Voltage Transformation Ratio and Duty Cycle for Different Turns Ratios

Another limitation of the PPC is the requirement of an isolated DC-DC converter topology. To demonstrate, the same analysis from the previous section is repeated for the PPC but without a transformer. Fig 3.5 shows the active switching stage without a transformer. When turned on, the bottom half of the diode bridge remains reverse biased and does not conduct. The input directly sources the current to the output as well as to the cap with only one path to the load. This creates an unnecessary current draw on the input and greatly impacts the converter efficiency. During the freewheeling stage, highlighted in Fig 3.6, a constant short is created in the converter that cycles through the diodes while trying to charge the capacitor in the active clamp.

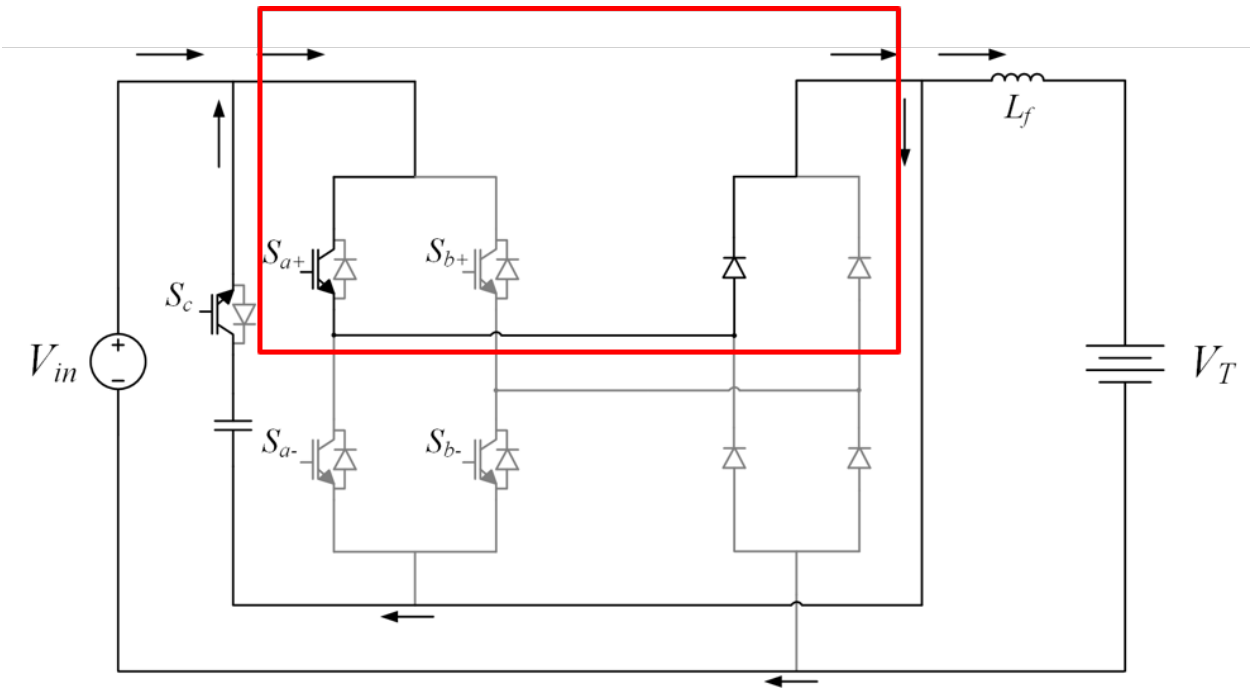

Figure 3.5: PPC Active Switch Stage Without Transformer

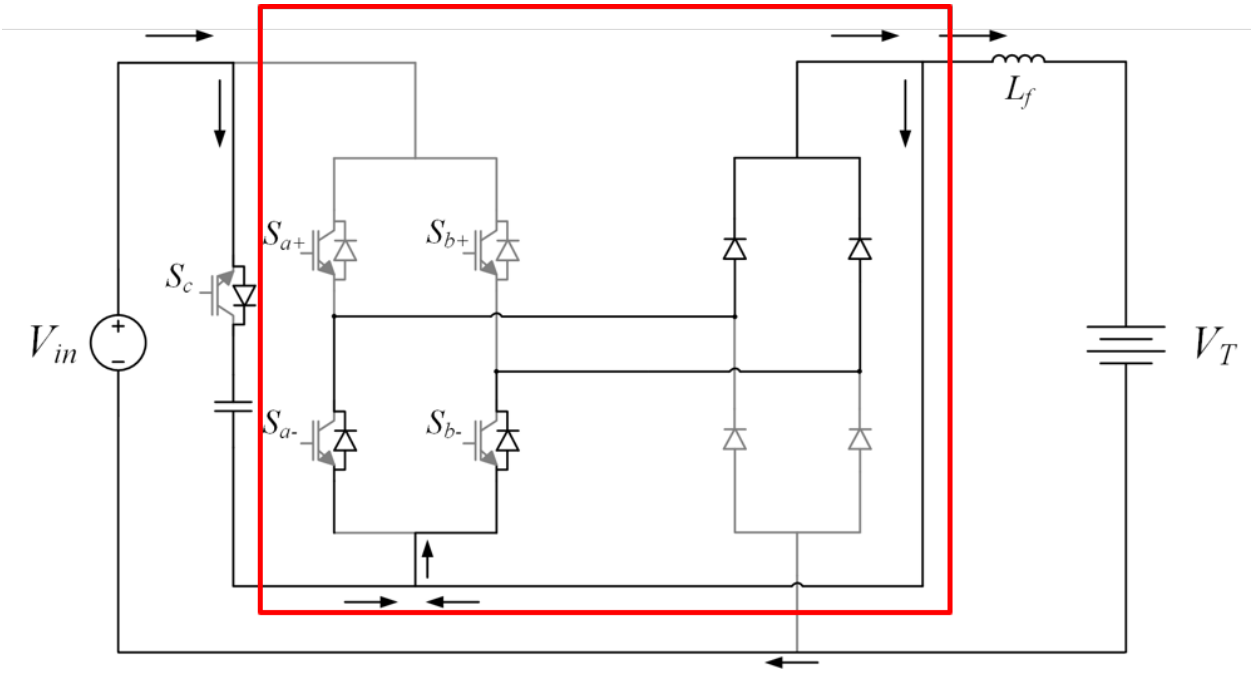

Figure 3.6: PPC Freewheeling Stage Without Transformer

3.4 PPC Control

The PPC uses a PI controller to regulate the current at the battery terminal. The current command, i_i^*, is given by a state of charge (SoC) based charging technique. The block diagram can be seen in Fig 3.7. There are a few SoC-based charging techniques applicable to XFC systems, with the most common technique being constant-current constant-voltage (CC-CV) due to its simplicity [30]. However, it has been shown that multistage constant-current charging (MSCCC) provides improvements over CC-CV in terms of charge time and temperature rise reduction with marginal improvements in efficiency [31][32]. This is due to the poor charging performance of the constant-voltage portion of the CC-CV charging profile. Fig 3.8 shows an example flow chart of the basic operation for MSCCC. Based on the initial SoC of the battery the appropriate constant-current stage is chosen. The SoC is then calculated based on the current going into the battery and its total capacity. The number of constant-current charging stages is chosen to be 5 as there are no significant benefits from adding more stages [31]. The first constant-current charging stage is chosen based on an appropriate cut-off voltage for the battery and the rated peak power of the converter given by

$$i_1 = \frac{P_{peak}}{V_{cut-off}} \tag{3.5}$$

The last constant-current stage is then chosen based on the desired cut-off voltage and the estimated battery characteristics at 80% state of charge and is given by

$$i_5 = \frac{V_{cut-off} - V_{oc}}{R_i + R_p} \tag{3.6}$$

With (3.5) and (3.6) chosen, the intermediate current stages can be solved as follows

$$i_3 = \sqrt{i_1 i_5} \tag{3.7}$$

$$i_2 = \sqrt{i_1 i_3} \tag{3.8}$$

$$i_4 = \sqrt{i_3 i_5} \tag{3.9}$$

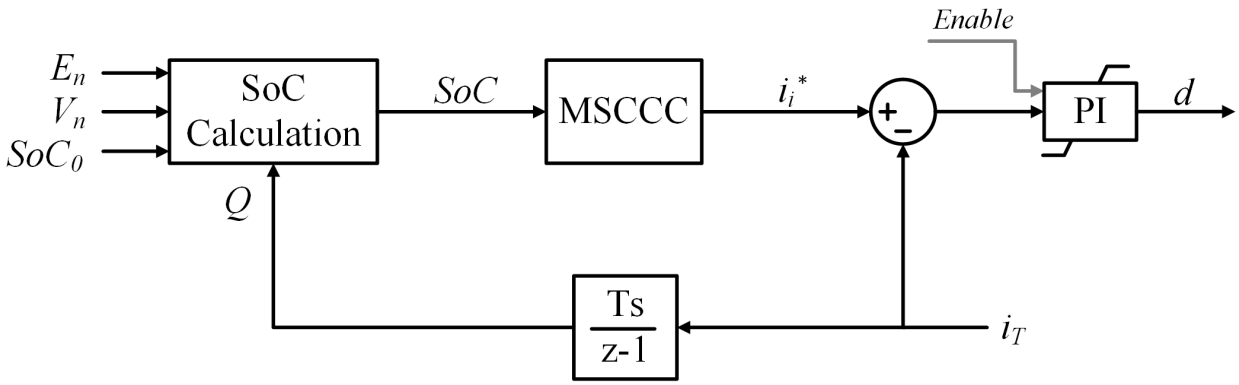

Figure 3.7: PPC Control Block Diagram

The gating signals are generated using a simple natural carrier symmetrical PWM operating in bipolar modulation. To generate the gating signal of the active clamp, the gating signals of switch legs A and B are compared using a XOR logical operator. The PWM operation created in Simulink can be seen in Fig 3.9.

3.5 Li-ion Battery Pack Model

To test the PPC modeling and control, a representative Li-ion battery model was developed using a 1st order RC network equivalent circuit model [33][34]. The circuit, shown in Fig 3.10, consists of the open circuit voltage, V_{oc}, the internal resistance of the battery, R_i, and an RC parallel network, R_p and C_p, to emulate the electrochemical dynamics. Li-ion batteries have a characteristic open circuit voltage profile that varies based on their SoC. Fig 3.11 shows the relationship that was used in this study which is based on a curve fitting of a Li-ion cell that was then scaled to reflect EV battery pack voltage levels.

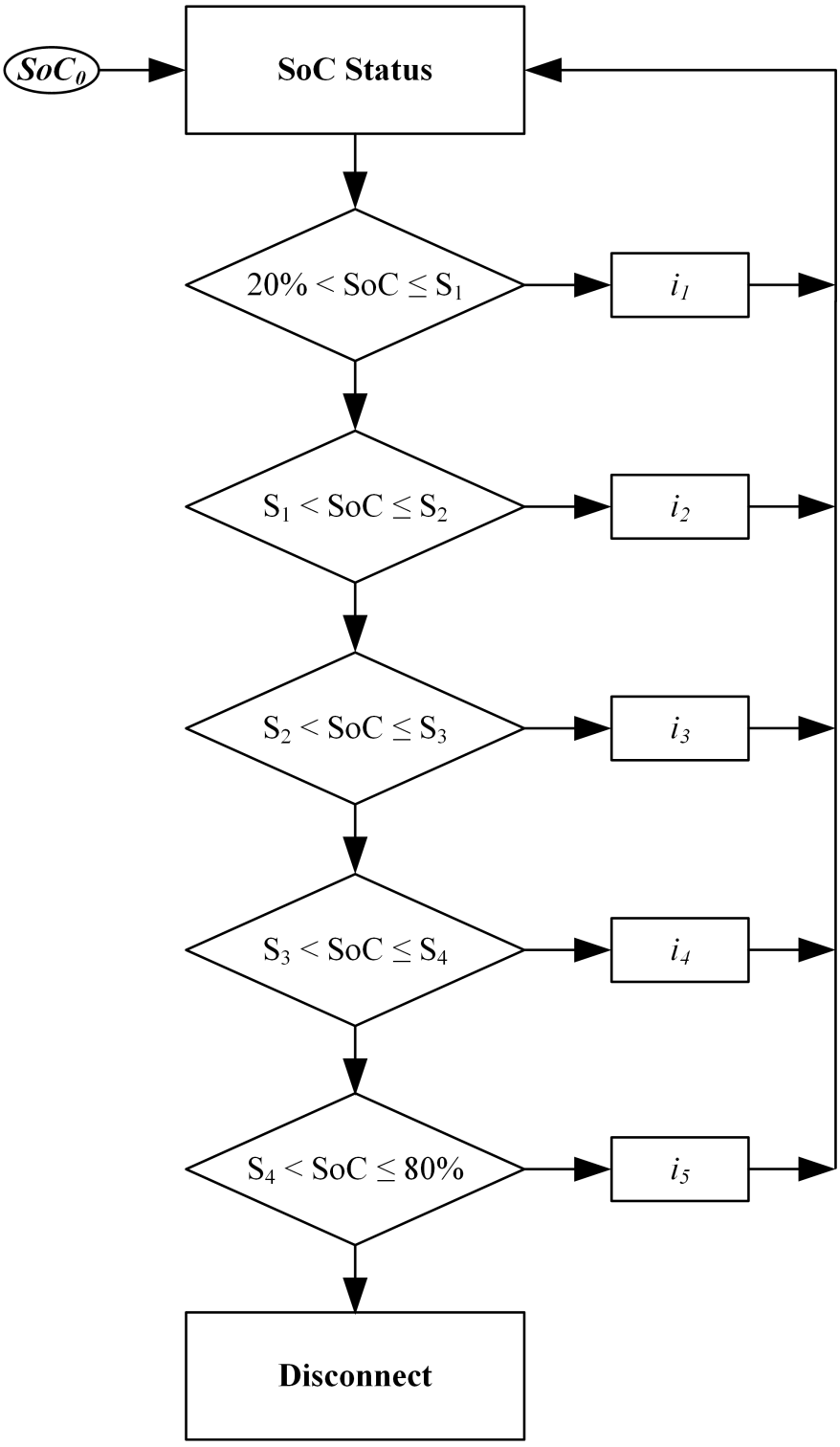

Figure 3.8: Multi-stage Constant Current Control Flow Chart

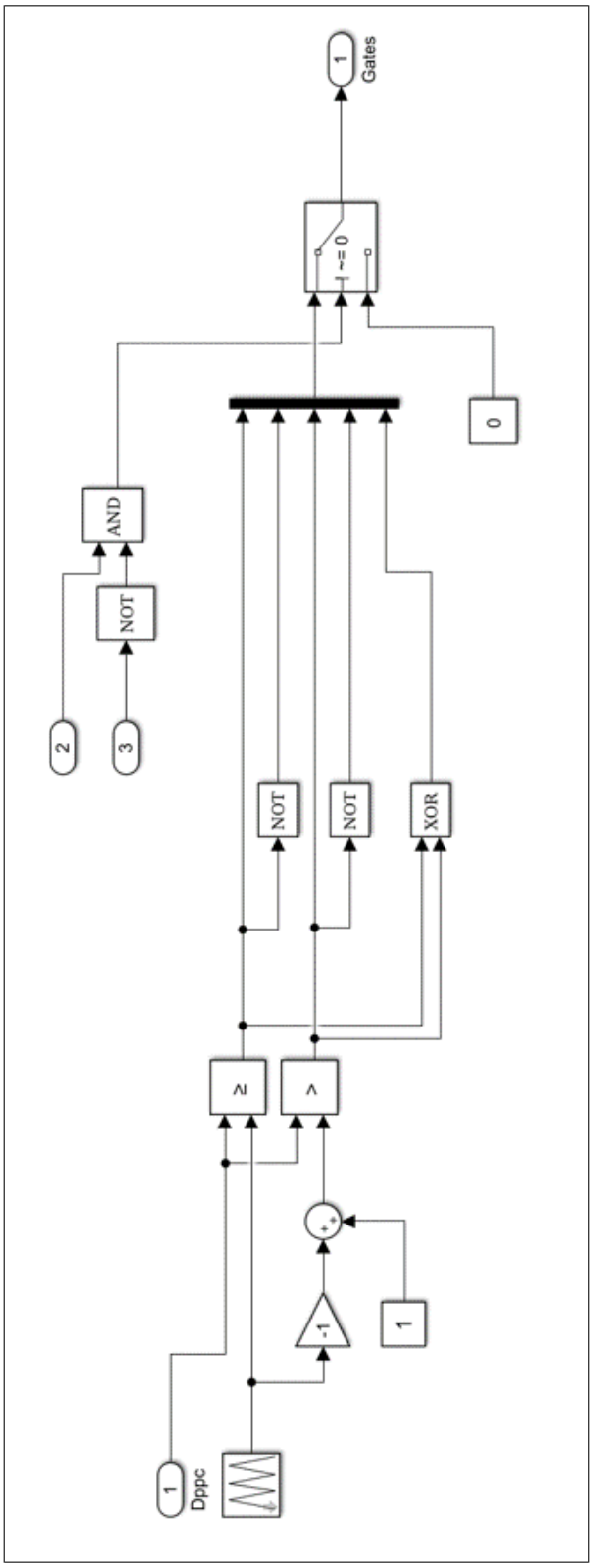

Figure 3.9: PPC PWM Generation

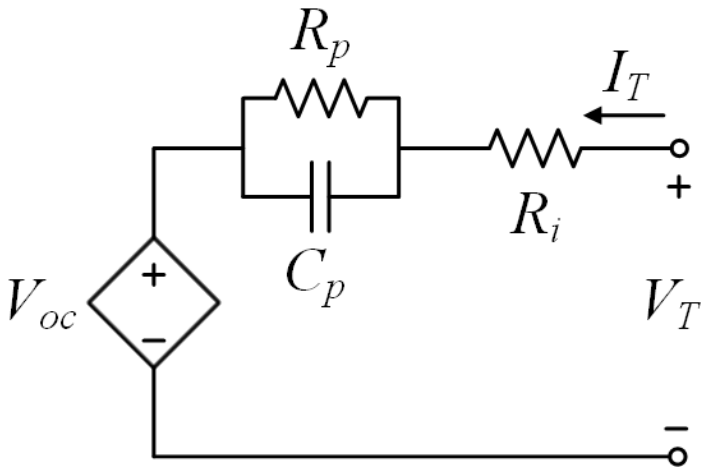

Figure 3.10: Li-ion Battery Equivalent Circuit Model

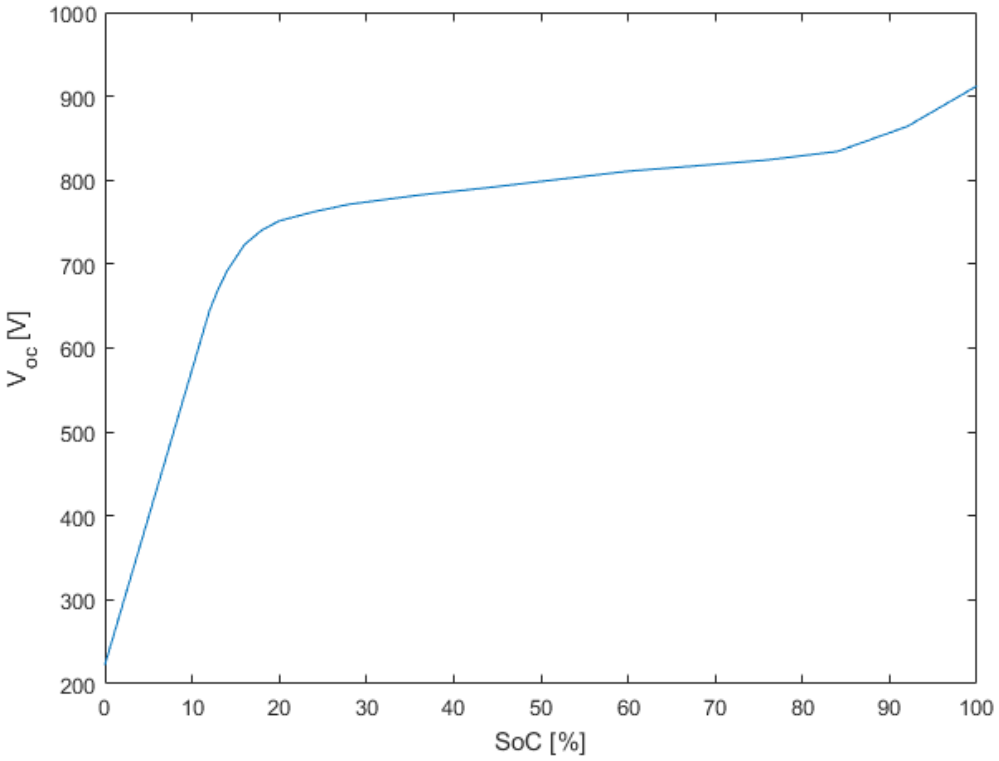

Figure 3.11: Relationship Between Open Circuit Voltage and State of Charge

CHAPTER 4
MEDIUM VOLTAGE INTERFACE

To supply high power demands that an XFC station would impose, a medium voltage connection to local distribution is chosen [35]. Forming the low voltage DC bus for the EV battery interfacing converters requires a step down in voltage, isolation from the grid, and voltage rectification. Typically, this would be done using a line frequency transformer (LFT) paired with either a diode or thyristor-based bridge rectifier. Although easy to implement, an LFT comes with many drawbacks. High power, medium voltage LFTs are physically large, are lossy operating at both rated and no-load conditions, and are static in operation. Additionally, the incoming power factor is left uncontrolled which can increase power losses and the station owner is likely to incur charges from the local utility. The SST, however, utilizes power electronics and high frequency transformers to replace the LFT at the interface of the grid. The SST provides active voltage regulation, galvanic isolation, power factor correction (PFC), and a DC output. By implementing an SST, the isolation and voltage conversion from the grid can be handled in a highly power dense, efficient, and flexible manner.

4.1 SST Topology

The SST, shown in Fig 4.1, is analyzed as consisting of two main stages. Each stage is independently controlled and classified as the input stage and the isolation stage. The input stage is an active rectifier composed of a cascaded H-bridge (CHB) multilevel converter. This stage interfaces with the MVAC grid to regulate the DC link voltage as well as control the input power factor. The isolation stage consists of multiple dual active bridge (DAB) converters that are connected in an input-series output-parallel (ISOP) configuration. This stage provides isolation from the grid and controls power flow to the LVDC bus. The ISOP configuration reduces the voltage level of the devices by N number of cascaded converters while sharing power through their paralleled outputs.

The SST in this application is designed to interface with a 13.8 kV, 60 Hz input voltage to form a 1 kV DC output bus with a power rating of 1.5 MVA.

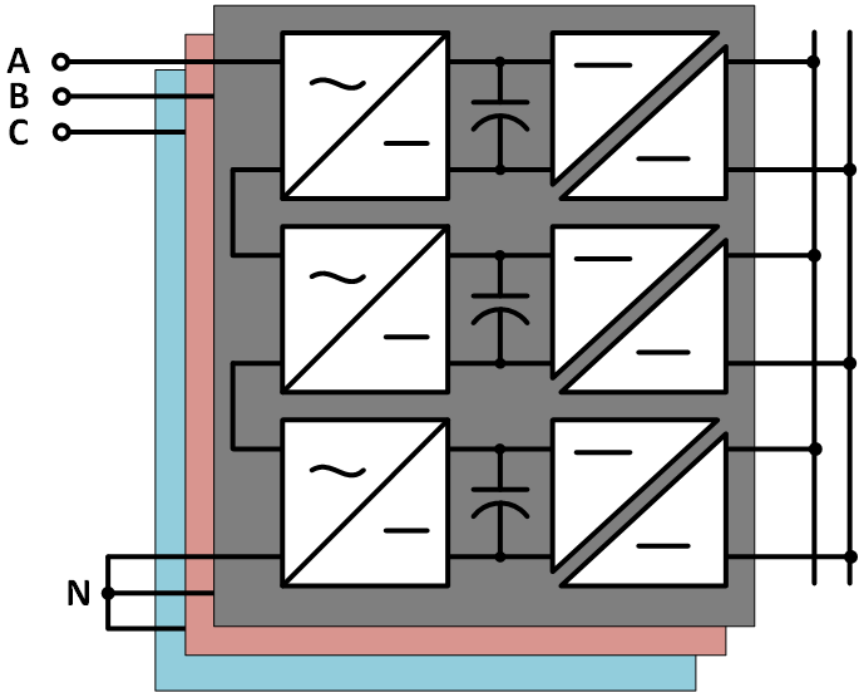

Figure 4.1: Grid Interfacing SST

4.2 CHB Modeling

Each CHB operates as a single-phase H-bridge with $2N + 1$ voltage levels per phase with the three phases connected in a wye configuration. Additionally, using the carrier phase shifted sinusoidal PWM (CPS-SPWM) technique with unipolar modulation creates an effective switching frequency equal to $2Nf_{sw}$. As a result, increasing the number of cascaded levels reduces stress on the switches and allows for smaller filtering components. However, increasing the number of switching levels reduces system reliability and adds complexity to the controls and communication channels. The CHB is chosen to have three cascaded H-bridges per phase to utilize emerging 6.5 kV voltage class SiC devices [36],[37]. The resulting input side waveform will consist of seven voltage levels. This will offer the benefits of a multi-level converter while keeping the system complexity relatively low. The switching frequency is chosen to be 3 kHz, producing an effective

switching frequency of 18 kHz ($2 \times 3 \times 3$ kHz). Because the system is designed to interface with a 13.8 kV grid connection, each CHB phase will have 8 kV single phase voltage as input. The cascaded DC link voltages are then regulated to be 4.5 kV.

4.3 Input Stage Control Strategy

The input stage control strategy, as seen in Fig 4.2, is divided into three parts with various feedback signals. The decoupled current control regulates the overall DC link voltage and input power factor. Voltage balancing needs to become part of the equation to handle any imbalances due to device losses or negative sequence voltages. To balance the average voltage across the nine DC link capacitors, there are two levels of balancing control. The first voltage balancing control can be described as interphase balancing which balances the average DC voltages between phases. Last is the intraphase balancing that balances the voltages of each cascaded H-bridge within one phase. To achieve the desired control objectives, measurements of the nine DC link capacitor voltages, grid side phase voltages, and grid side phase currents need to be taken as feedback. Additionally, a phase-locked loop (PLL) must be implemented to synchronize the control signals with the phase angle, θ, of the grid.

4.4 Decoupled Current Control

Decoupled current control is a common control technique used for grid tied voltage source converters (VSC). It is based on the Park transformation which converts three phase signals into the d-q rotating reference frame given by

$$\begin{bmatrix} u_d \\ u_q \end{bmatrix} = \frac{2}{3} \begin{bmatrix} cos(\theta) & cos\left(\theta - \frac{2\pi}{3}\right) & cos\left(\theta + \frac{2\pi}{3}\right) \\ -sin(\theta) & -sin\left(\theta - \frac{2\pi}{3}\right) & -sin\left(\theta + \frac{2\pi}{3}\right) \end{bmatrix} \begin{bmatrix} u_a \\ u_b \\ u_c \end{bmatrix} \tag{4.1}$$

Within the d-q reference frame, the control signals can be easily controlled using traditional PI controllers. Using the θ obtained from the PLL, the grid side voltage and current measurements

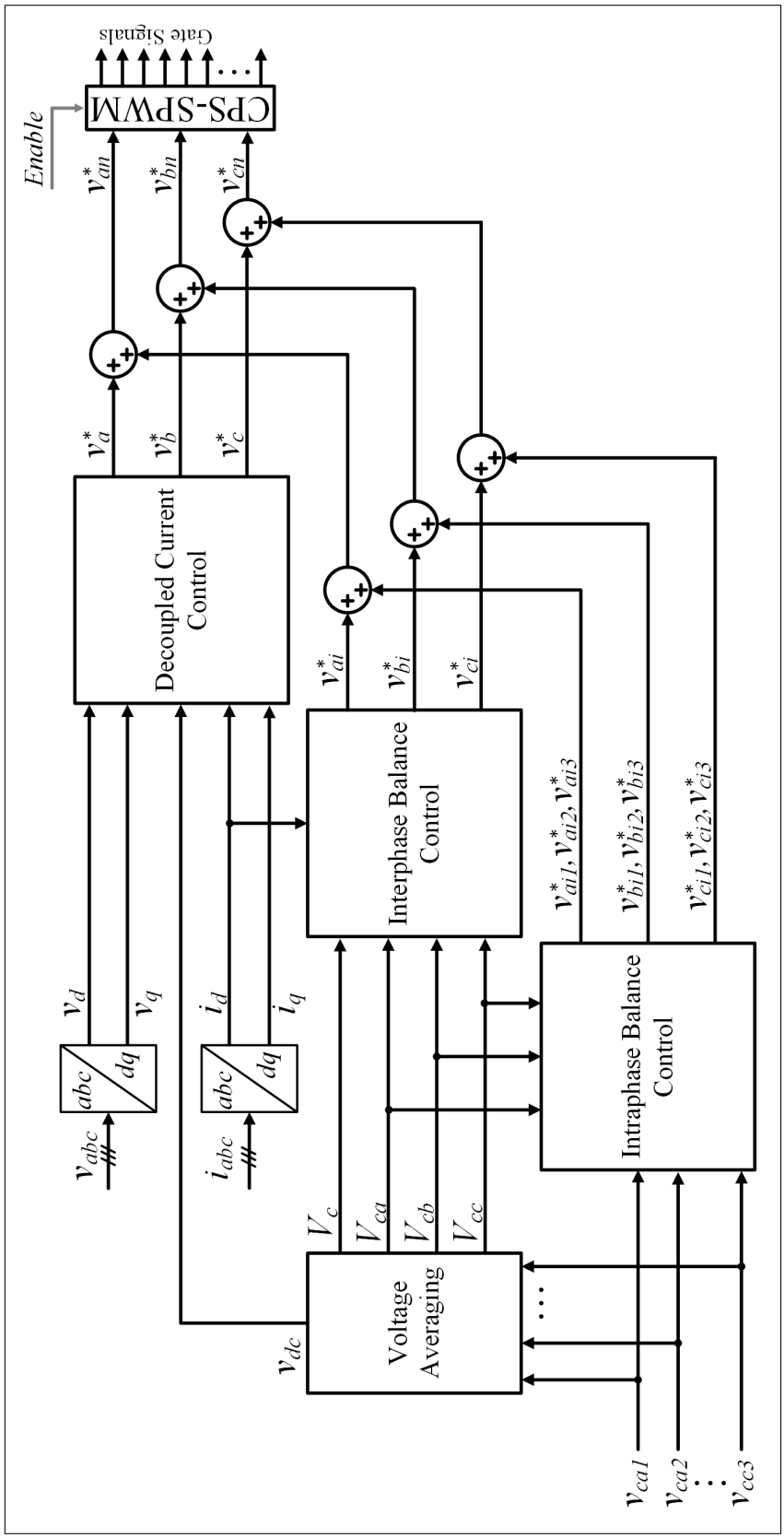

Figure 4.2: Input Stage Control Strategy

are transformed to the d-q reference frame. In the d-q reference frame, the d-axis is related to the active power flow and the q-axis pertains to the reactive power flow. Fig 4.3 gives the block diagram in which the controls are realized. A voltage command is set to the desired overall DC link voltage to be compared with the sum of all nine DC link capacitors given by

$$v_{dc} = \frac{1}{3}(v_{c_{a1}} + v_{c_{a2}} + ... + v_{c_{c3}}) \tag{4.2}$$

The error from (4.2) is fed through a traditional PI controller to generate the d-axis current command, i_d^*. For this application of unidirectional power flow, the q-axis current command, i_q^*, is set to be zero. This corresponds to a unity power factor which avoids any related power loss as well as possible penalties incurred from the local utility for low power factor. The decoupling factor ωL_{ac} takes into consideration the grid side AC filter inductance between the converter input and grid connection. The d-axis voltage and q-axis voltage commands are generated to be transformed back to the ABC reference frame via the inverse Park transformation for the final three phase voltage commands.

4.5 Interphase Voltage Balance

As mentioned, the interphase balancing control balances the average DC link voltages between the three phases. To achieve this, the active current is redirected to or away from the DC link capacitors to raise or reduce their voltages. There are a few different approaches that have previously been used in literature. For delta configured systems, a common technique is to utilize the zero sequence current to adjust capacitor voltages [38],[39]. For wye configured systems, however, there is not a zero sequence current so an alternative method must be used. In [40], the current decoupling is incorporated into the voltage balance control and balancing is achieved through cascaded PI controllers. With the current decoupling controlled independently, the balancing control becomes much simpler. In [41] and [42], the voltage balancing is handled using cascaded proportional controllers that use the average DC link voltage and active current, i_d, as feedback. Without

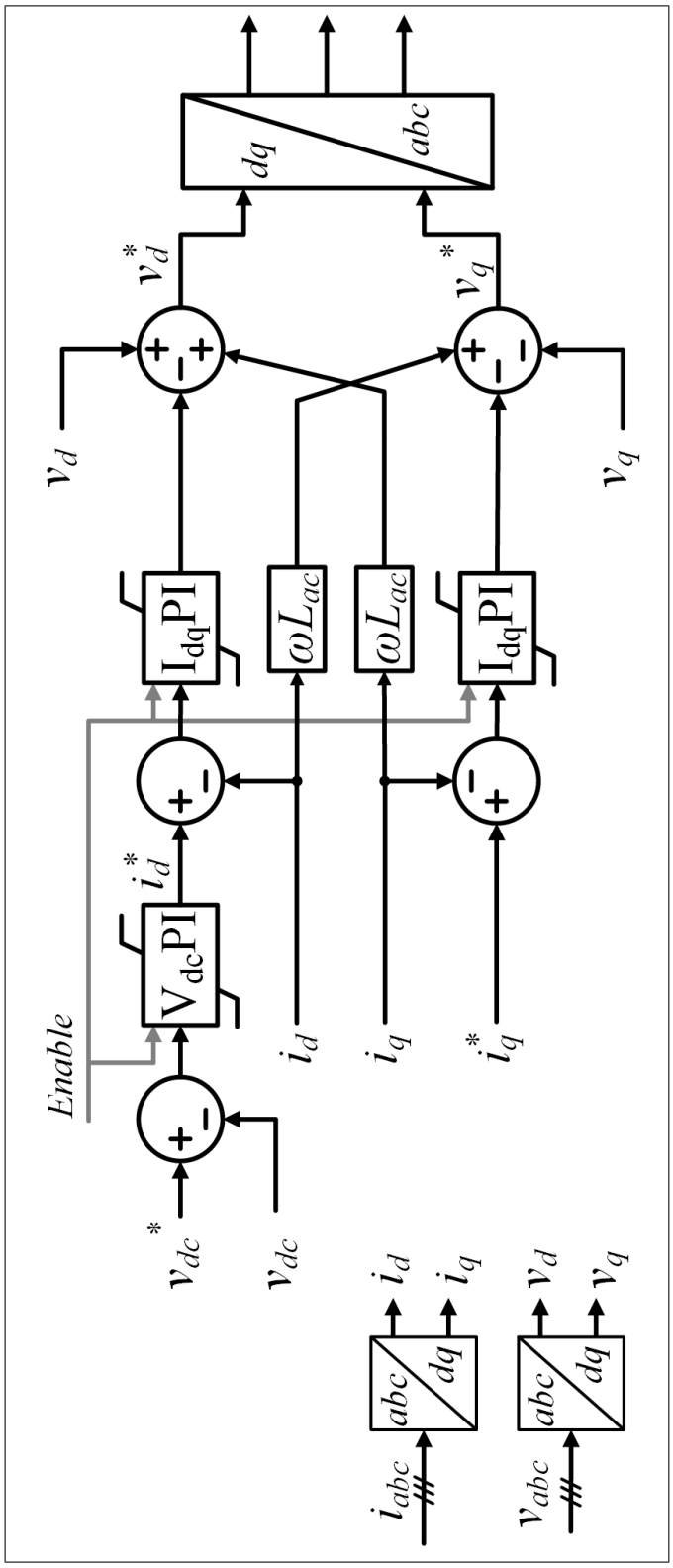

Figure 4.3: Decoupled Current Control Block Diagram

integral action, however, the balancing control is susceptible to steady-state errors. For this reason the balancing control is chosen to be a single PI stage used as a voltage regulator. Fig 4.4 contains the block diagram of the balancing control for each phase. The average DC link voltage of each phase is calculated as (4.3) and the average of the three phases as (4.4)

$$V_{c_a} = \frac{1}{3}(v_{c_{a1}} + v_{c_{a2}} + v_{c_{a3}}) \tag{4.3}$$

$$V_c = \frac{1}{3}(V_{c_a} + V_{c_b} + V_{c_c}) \tag{4.4}$$

The error between (4.3) and (4.4) is then fed through a PI controller. The balancing signal is then multiplied by $cos(\theta)$, with θ being the phase obtained from the PLL. This performs a single phase inverse d-q transformation which places the signal in phase or 180° out of phase with the voltage command generated by the decoupled current controller. By adding the signals in this manner, the modulation signal can be adjusted in magnitude to increase or decrease phase current without imposing any phase shift. This is then repeated for each phase, substituting θ with $\theta - 2\pi/3$ and $\theta + 2\pi/3$ for phases b and c, respectively. It should be noted that the performance of the PI controller can be improved by applying a low pass or notching filter to the feedback signals of each phase. Since each phase acts as a single phase H-bridge converter operating under unipolar modulation, there is a significant second harmonic. If left unfiltered, this 120 Hz component can make the otherwise DC feedback signal appear sinusoidal, degrading performance.

4.6 Intraphase Voltage Balance

The intraphase voltage balancing control balances the individual DC link voltages of every H-bridge with the average voltage within each phase. There are many different approaches to achieve individual voltage balance [43],[44],[45]. In [43] and [44], the focus is on functionality during bidirectional operation. There are many strategies proposed in [45] which focuses on operating modes such as inductive and capacitive modes. Because this system is chosen to be unidirectional with unity power factor, the operating principle is similar to the interphase balancing outlined in the

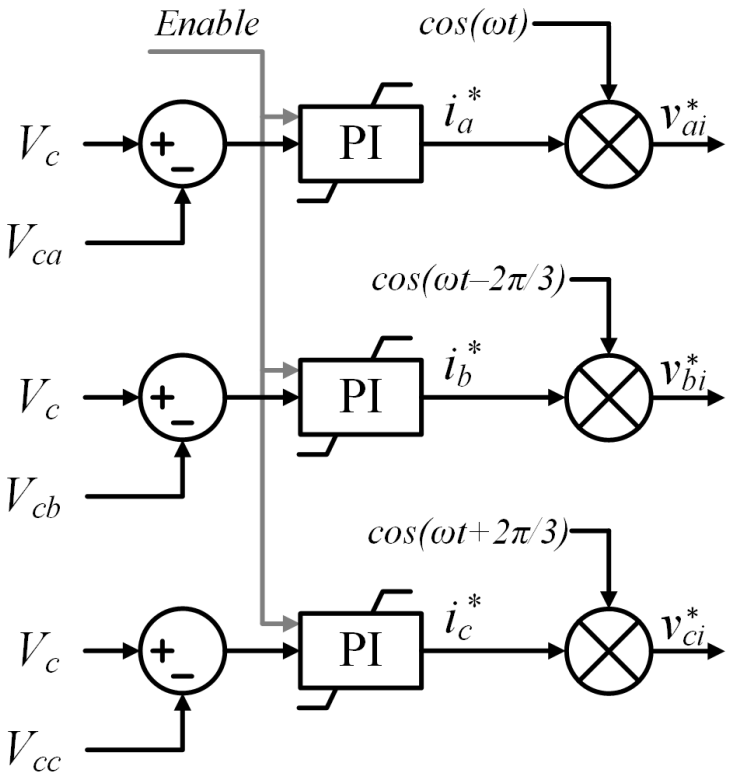

Figure 4.4: Interphase Balance Control Block Diagram

previous section. Fig 4.5 shows the block diagram for the phase A voltages. To achieve balancing on the individual level, active current is distributed within each phase by adjusting the amount of time each H-bridge is active. The intraphase balancing controller is purposely undertuned in comparison with the interphase balance so as to avoid conflicting controls. In this sense, the interphase balance is seen as the inner current loop while the intraphase is considered as the outer voltage loop. As with the interphase balancing, the output of the PI controller is multiplied by $cos(\theta)$ to place the individual modulation signals in phase or 180° out of phase with the summed voltage commands of the previous levels of control. Fig 4.6 highlights this in the next section. Repeating this technique for the remaining phases then generates a separate switching signal for each H-bridge in the system.

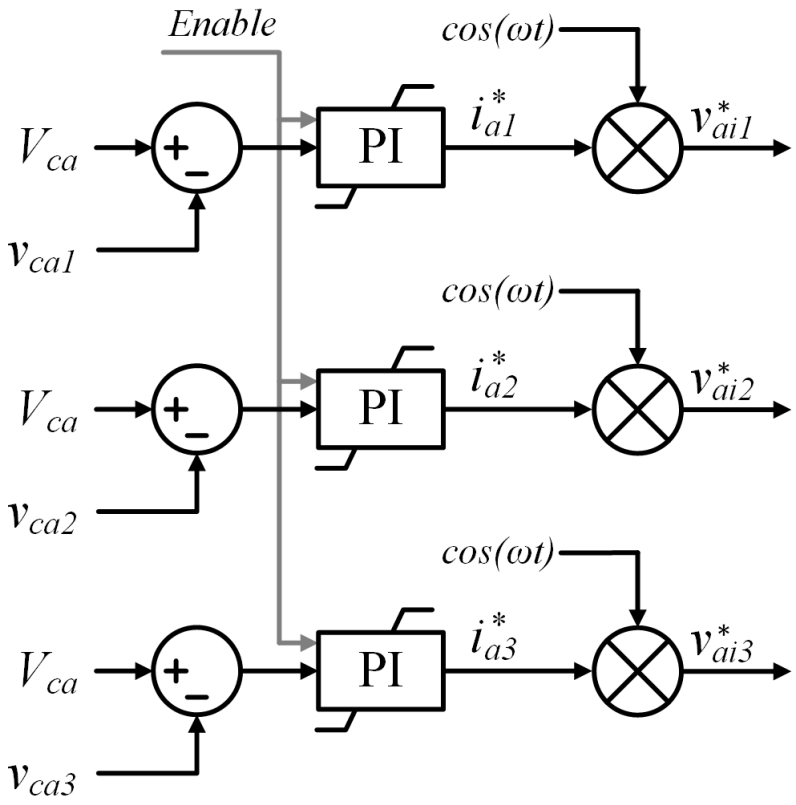

Figure 4.5: Intraphase Balance Control Block Diagram

4.7 Carrier Phase Shifted Sinusoidal PWM

Perhaps one of the most common techniques of generating gate signals for the CHB is CPS-SPWM [46],[47]. The CPS-SPWM method is simply a modified version of sine-triangle PWM which accounts for the number of cascaded converters within a single phase. Fig 4.6 shows the modulation waveforms of a single phase. Each cascaded converter within the phase is represented by a triangular carrier waveform. The carrier waveforms operate at the set switching frequency but are staggered in phase by $2\pi/N$. This interleaving of the carrier waveforms is what creates an "effective" switching frequency of $2Nf_{sw}$. For unipolar modulation, the sinusoidal modulation signals have an equal and opposite signal to be superimposed on the carrier waveforms to generate gate signals for each phase. In the case of a voltage imbalance within a phase, each cascaded converter has its own modulation signal that varies in magnitude. The resulting modulation redi-

rects the active current to or from their respective DC link capacitor. This same procedure is then repeated for the remaining two phases with the sinusoidal modulation signal being phase shifted by $\pm 2\pi/3$ and varied in magnitude to handle any voltage imbalances.

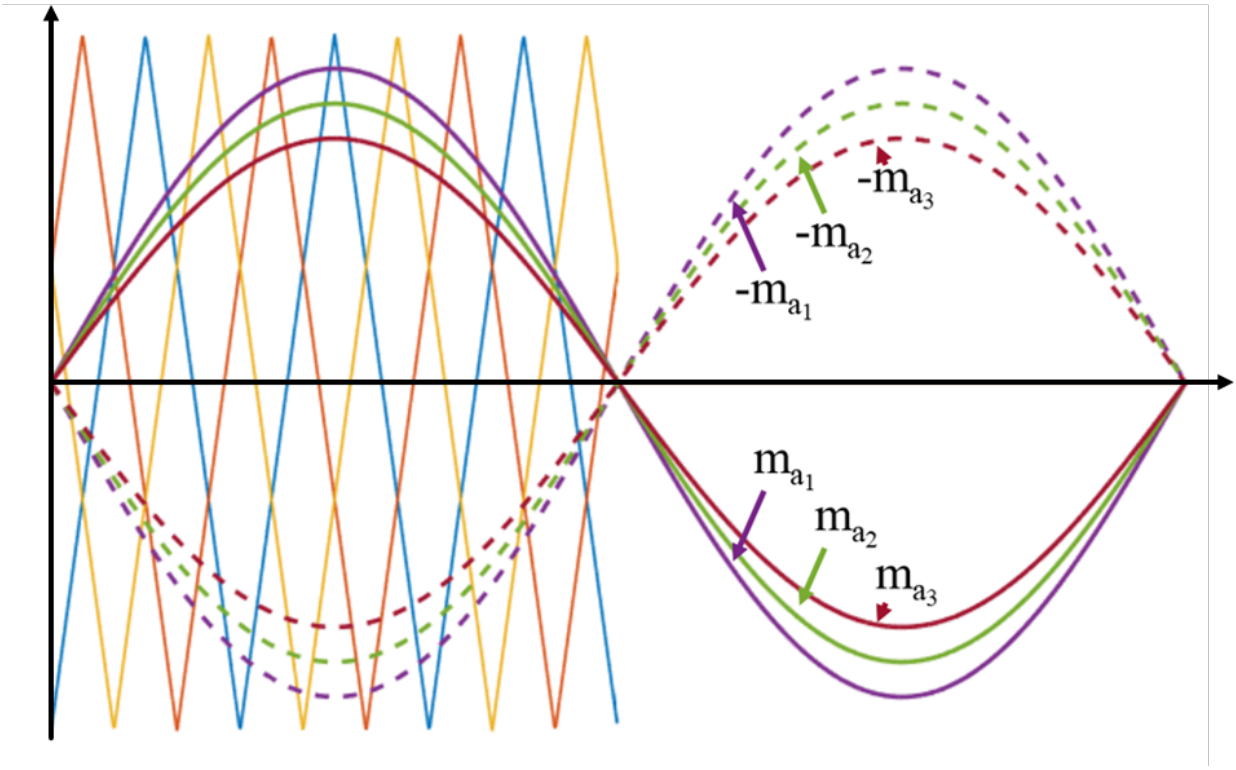

Figure 4.6: CPS-SPWM of Phase A in Unbalanced Conditions

4.8 DAB Modeling

The DAB circuit, shown in Fig 4.7, is an isolated DC-DC converter that consists of two H-bridges placed on both sides of a high frequency transformer. Both the primary and secondary side H-bridges are operated with a bipolar modulation at 50% duty cycle. The square wave voltages on the primary and second sides induce a current through the leakage inductance of the transformer as shown in Fig 4.8. The average power through the transformer can then be controlled by introducing a phase shift, δ, between the primary and secondary side switching signals and is described by

$$P_o = \frac{nV_{pri}V_{sec}}{2L_{lk}f_{sw}}d(1-d) \tag{4.5}$$

where L_{lk} is the leakage inductance, f_{sw} is the switching frequency, and the phase shift, δ, is represented by

$$\delta = d\pi \tag{4.6}$$

It can be seen from (4.5) and (4.6) that the maximum power output of the DAB occurs when $\delta = \pi/2$. Power flows from the leading-phase side to the lagging-phase side, so by choosing a phase shift in the range $-\pi/2 \leq \delta \leq \pi/2$ the DAB gains bidirectional functionality. For use in the XFC station, however, the DAB is operated unidirectionally and δ is limited to $0 \leq \delta \leq \pi/2$. Depending upon application, the transformer turns ratio can be used to set the voltage level going from primary to secondary. For this system, the transformer is being used as a step-down transformer with a turns ratio $4.5 : 1$. With the voltages set on the primary and secondary, the leakage inductance of the transformer can be then be chosen based on the maximum power output given by

$$L_{lk} = \frac{nV_{pri}V_{sec}}{8P_{max}f_{sw}} \tag{4.7}$$

The output-parallel configuration shares the current output of the nine DAB converters to provide power to the LVDC bus.

4.9 DAB Control

To control each DAB, a voltage regulator is used to generate the appropriate phase shift on the secondary. Fig 4.9 shows the control block diagram of one DAB which simply uses a PI controller to produce the control signal, d. The gating signals are then generated by level shifting sawtooth carrier waveforms by $\pm d$ about zero. The level shift then creates a phase delay in the zero crossing of the rising edge, as shown in Fig 4.10. With rising edge zero crossing detection, this phase delay creates the phase shift, δ, between primary and secondary switching signals. To operate with 50% duty cycle, the same procedure is done but with another pair of sawtooth waves phase shifted by half of the switching period. An SR flip flop is then used to hold the detection pulse of the first pair of sawtooth waveforms and is reset with the second pair of sawtooth waveforms. The full PWM

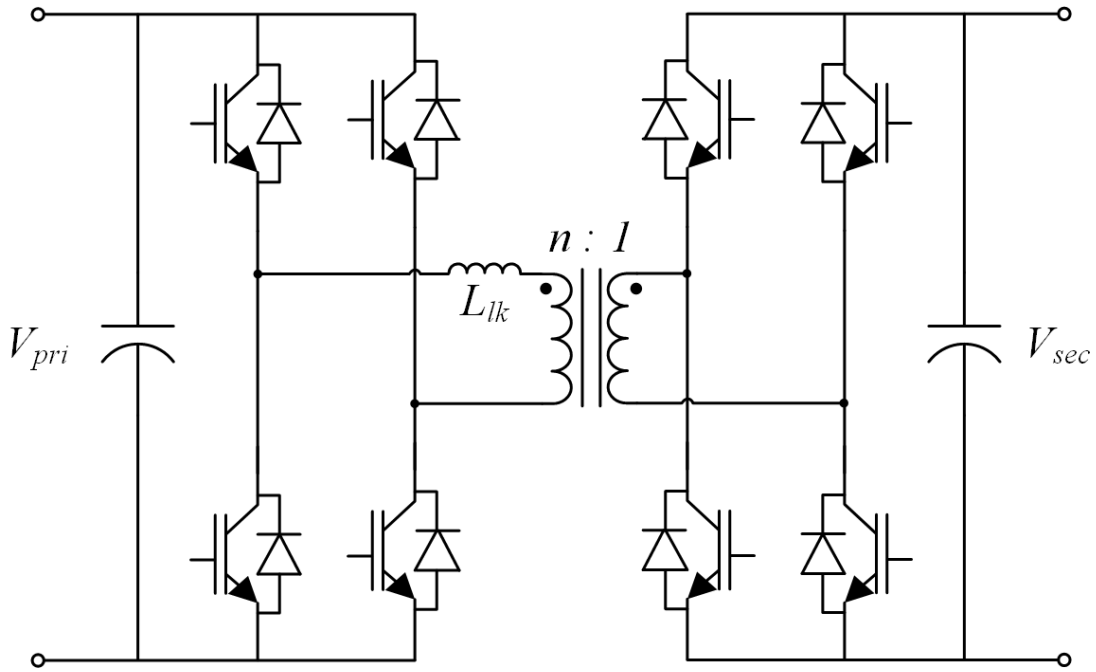

Figure 4.7: DAB Converter

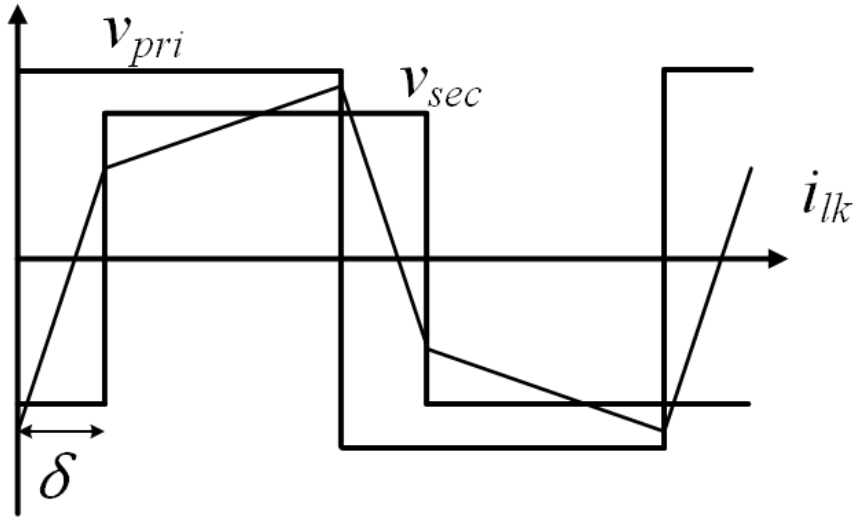

Figure 4.8: Waveforms of DAB Operation

operation created in Simulink can be seen in Fig 4.11.

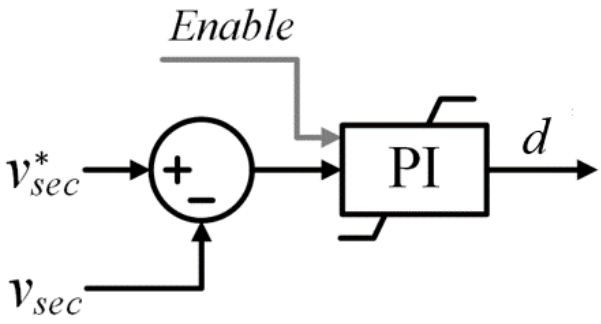

Figure 4.9: DAB Controller

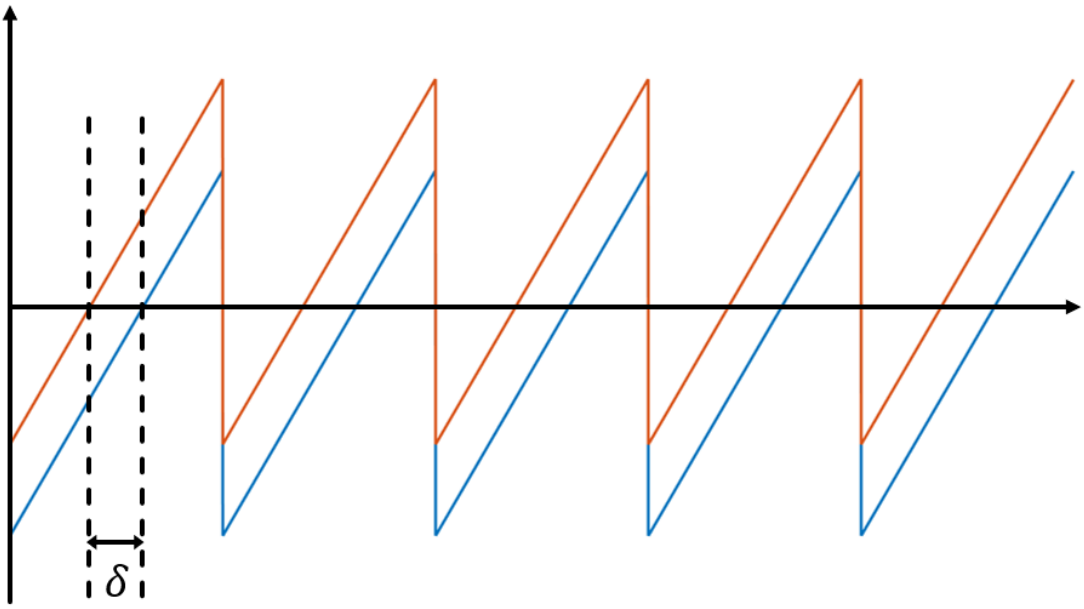

Figure 4.10: DAB PWM Carrier Waveforms

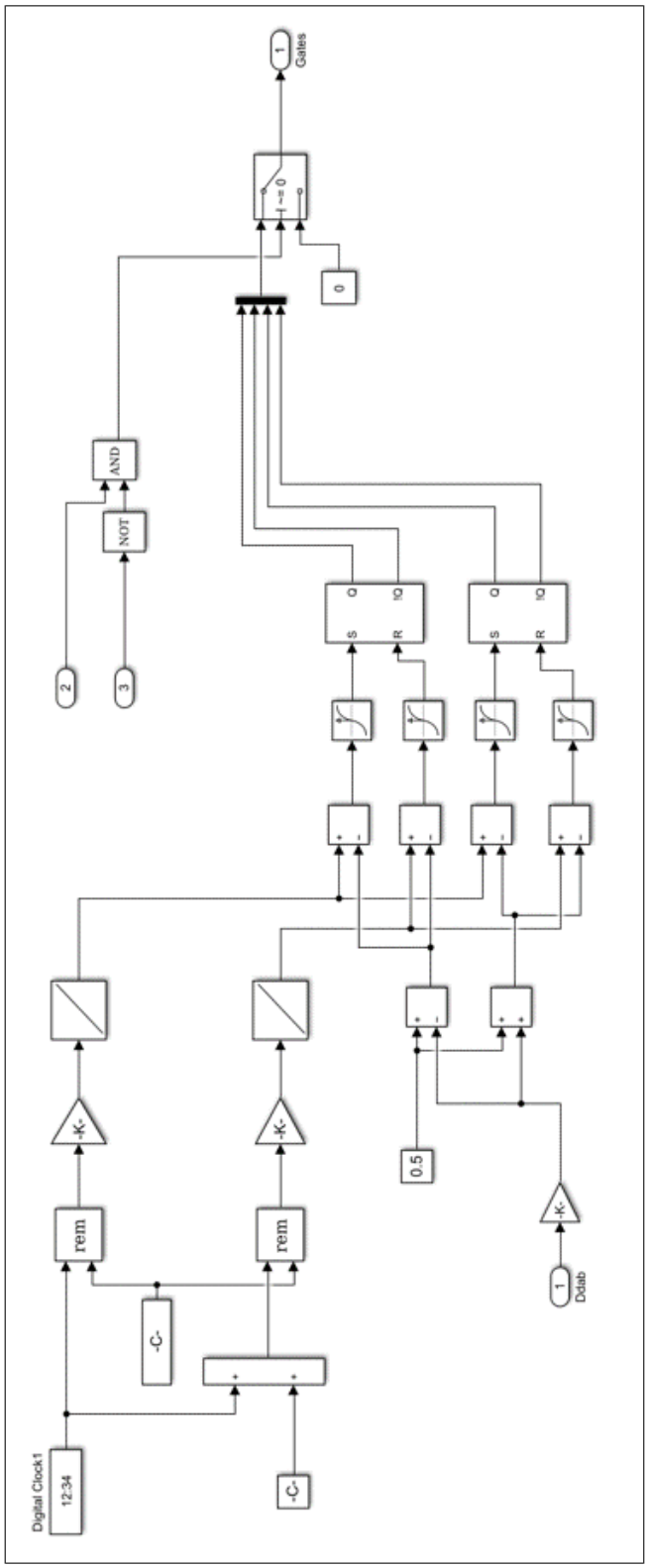

Figure 4.11: DAB PWM Generation

CHAPTER 5

SYSTEM SIMULATION RESULTS

To verify the performance of the system, various simulations are conducted within a MATLAB/Simulink environment combined with the PLECS blockset. The electrical components of the system are constructed using the PLECS blockset, and the control system and analysis are done in MATLAB/Simulink. The simulated system consists of switching models of nine CHBs, nine ISOP configured DABs, and two PPCs connected at the LVDC bus.

Table 5.1: Simulated SST Parameters

Parameter	Value
Input Line to Line Voltage	13.8kV
Input Line Frequency	60Hz
Rated Power	1.5MVA
Number of Cascaded Levels	3
MVDC Voltage	4.5kV
LVDC Voltage	1kV
Switching Frequency CHB	3kHz
Switching Frequency DAB	10kHz

5.1 Verification of System Start-up

To establish the MVDC bus at the output of the CHB, a series of steps must take place to ensure a safe transition from start-up. Before energizing the system, all switching converters are disabled. A pre-charge resistor is added between the grid and the rest of the system to limit the in rush current transient on start up. After the DC bus voltage reaches a certain voltage level and a predetermined amount of time passes, a contactor closes to bypass the pre-charge resistance. The switching devices of the CHB remain off while the DC link capacitors continue to charge through the anti-parallel diodes. After reaching an equivalent diode-rectified voltage, the CHB receives a ramping voltage command to begin boosting to the desired bus voltage. For verification, the

MVDC bus voltage and power input are monitored for the following steps which are highlighted in Fig 5.1.

1. The system is energized and starts in the pre-charge state.
2. Pre-charge ends and the system is connected directly to the grid. The system quickly reaches the diode-rectified voltage level.
3. Active rectifier is enabled and the CHB receives a ramping voltage command.
4. The MVDC bus reaches the desired voltage.

5.2 Demonstration of Voltage Balancing

To first demonstrate the interphase voltage balancing control of the CHB, a forced imbalance is created by applying different valued resistors in parallel with the DC link capacitors. The system is run without balancing control until a steady state is reached. At 2 s, the interphase balancing control is applied. Fig 5.2 shows the average DC voltages quickly reach the averaged reference voltage. To demonstrate the combined interphase and intraphase voltage balancing control and how the two interact, a similar test is conducted. In addition to the interphase imbalance, an additional resistor imbalance is applied within phase A. Referring to Fig 5.3, the combined balancing control is enabled at 2.5 s. The interphase balance immediately responds to balance the average voltages between phases. At about 2.65 s, focusing on v_{a_3}, you can see the intraphase balancing take over to correct the individual voltages of phase A. Because the voltage balancing is redirecting active power, power quality issues may arise on the input side if the imbalance is large enough. Furthermore, this voltage balancing technique cannot function properly if the system is already operating at or near rated power. This presents an opportunity to add power balancing to the DAB control to redistribute the power imbalance. Fig 5.4 shows that even though there are power quality issues, the average power factor remains at unity under unbalanced conditions. It should be noted, however, that this is an exaggerated condition to display the control effectiveness. In practice, the voltage balancing would be compensating for small discrepancies between component values.

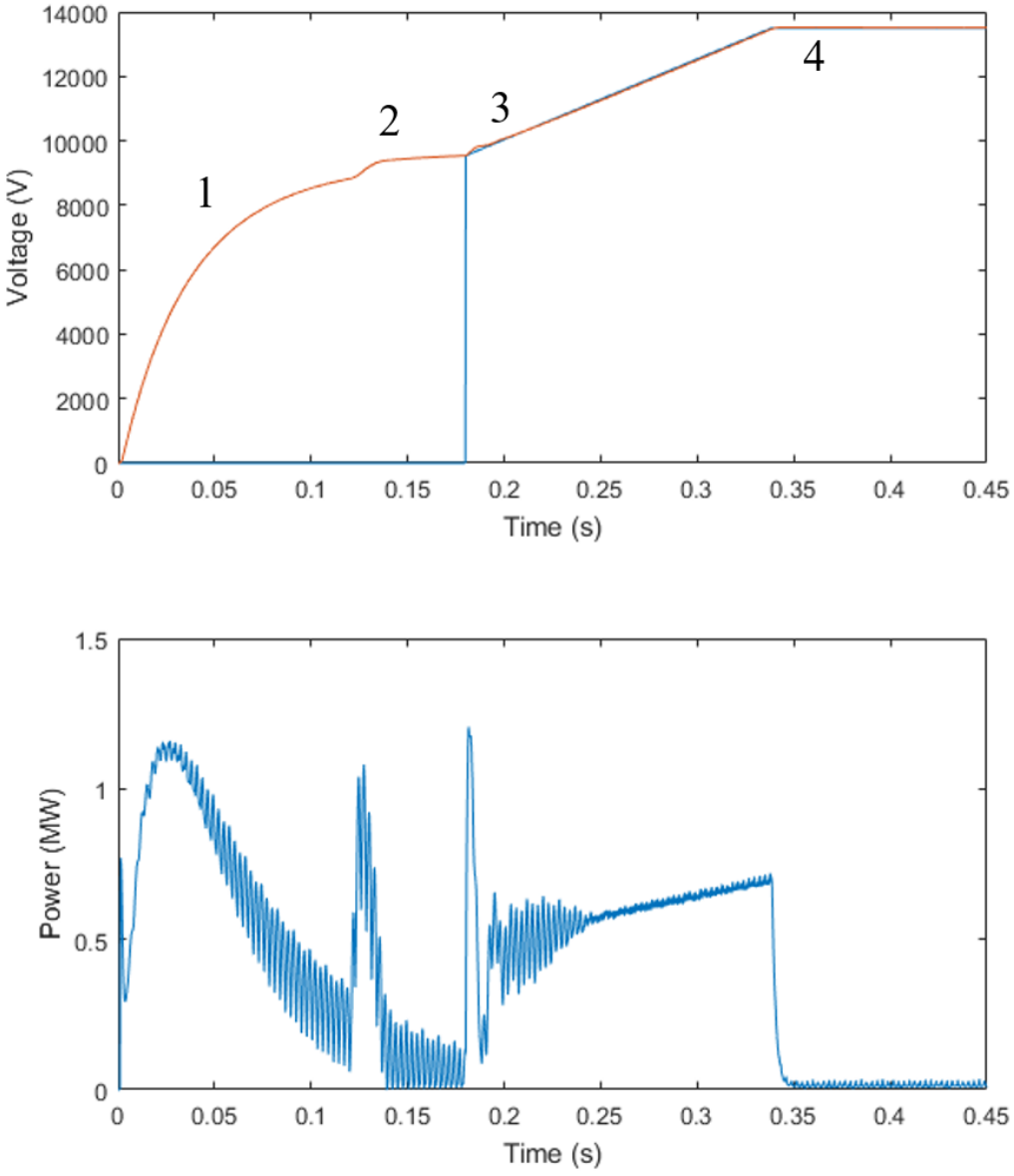

Figure 5.1: System Start-up Stages

5.3 Battery Charging Plan

To simulate the MSCCC charging technique of an EV battery, a separate simulation of the PPC is used in PLECS standalone. The PPC charger values used are given in Table 5.2. The result is shown in Fig 5.5. The EV battery is connected at 65% SoC which is still in the range of the i_1

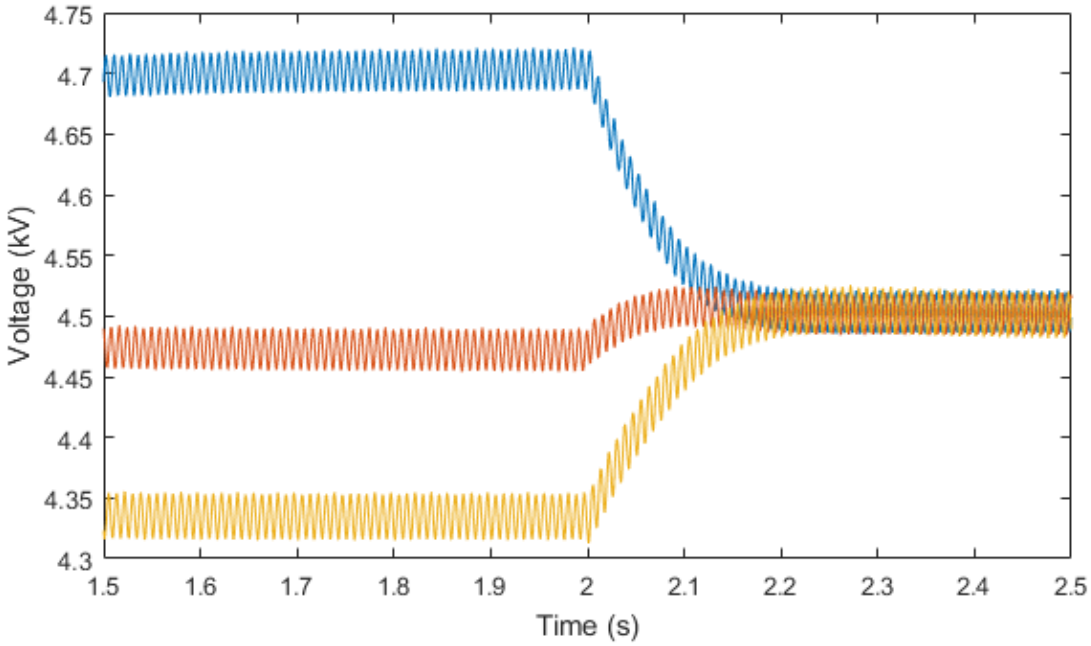

Figure 5.2: Average DC Link Voltages Per Phase With Interphase Voltage Balancing Control

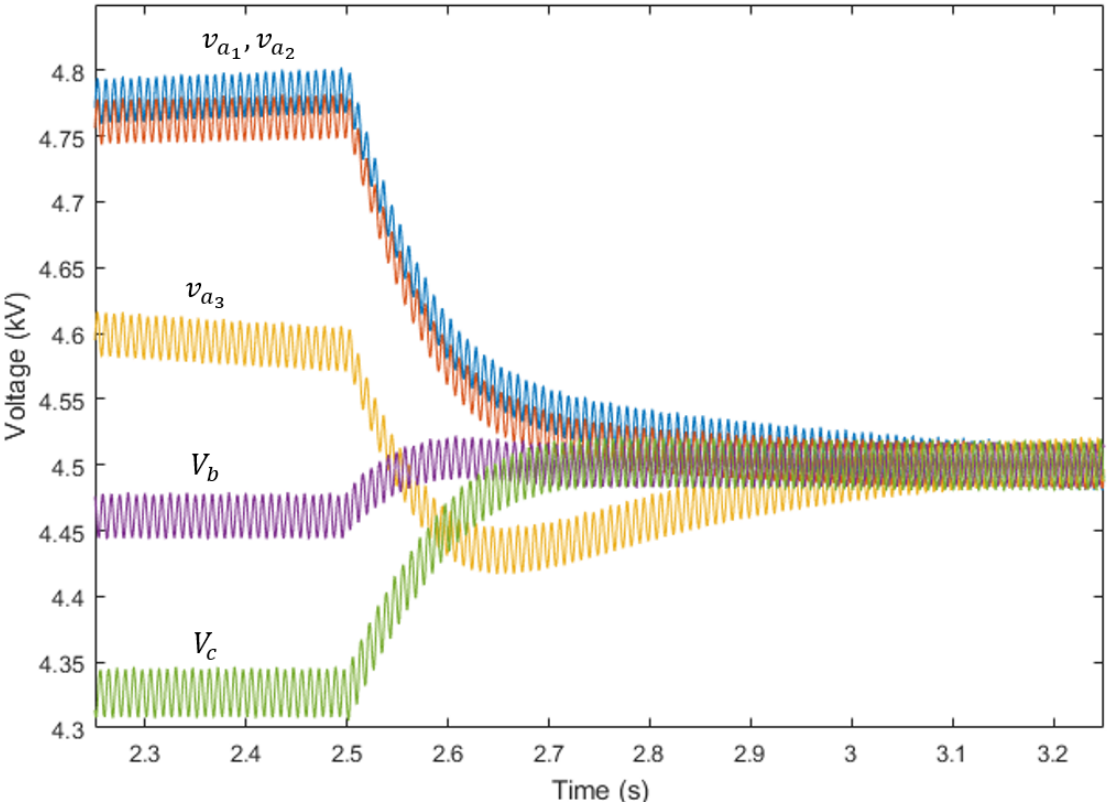

Figure 5.3: DC Link Voltages With Combined Voltage Balancing Control

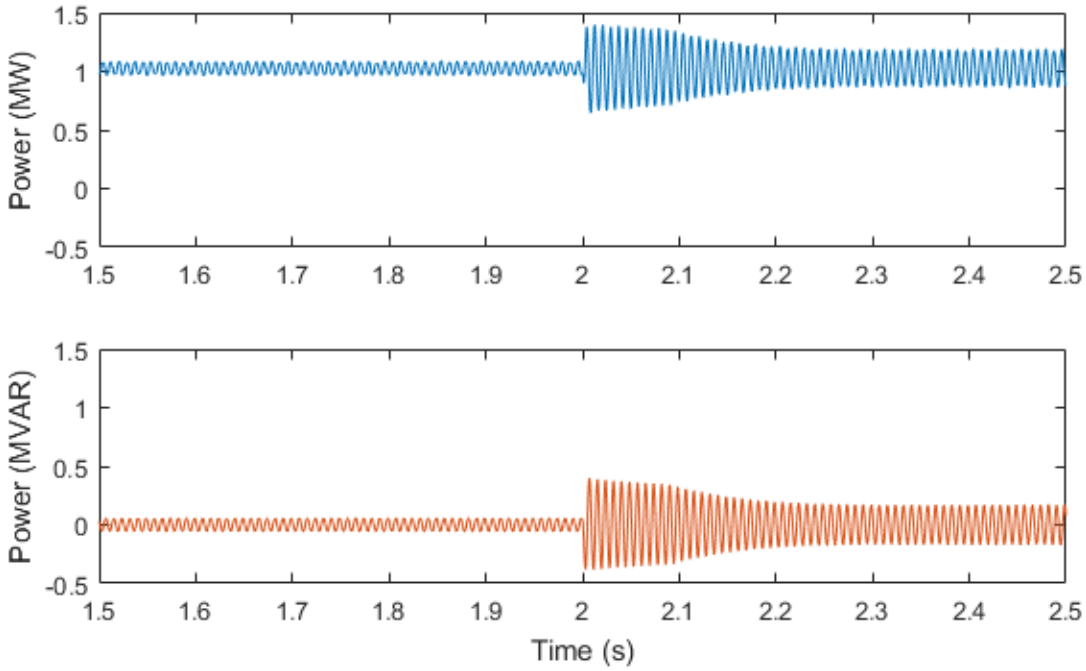

Figure 5.4: Input Real and Reactive Powers During Unbalanced Conditions

constant current level. The battery continues to charge with constant current i_1 as it approaches the cut-off voltage of the battery terminal. The constant current command drops to i_2, lowering the terminal voltage. Again, the battery continues charging as it approaches the cut-off voltage. This process repeats for the remaining constant current stages through i_5. Once the EV battery reaches a full charge of 80% SoC the current is regulated to zero for the battery to be disconnected.

Table 5.2: Simulated PPC Charger Parameters

Parameter	Value
Input Voltage	1kV
Battery Terminal Voltage	770-835V
Rated Peak Battery Power	350kW
Transformer Turns Ratio	7
Switching Frequency	20kHz

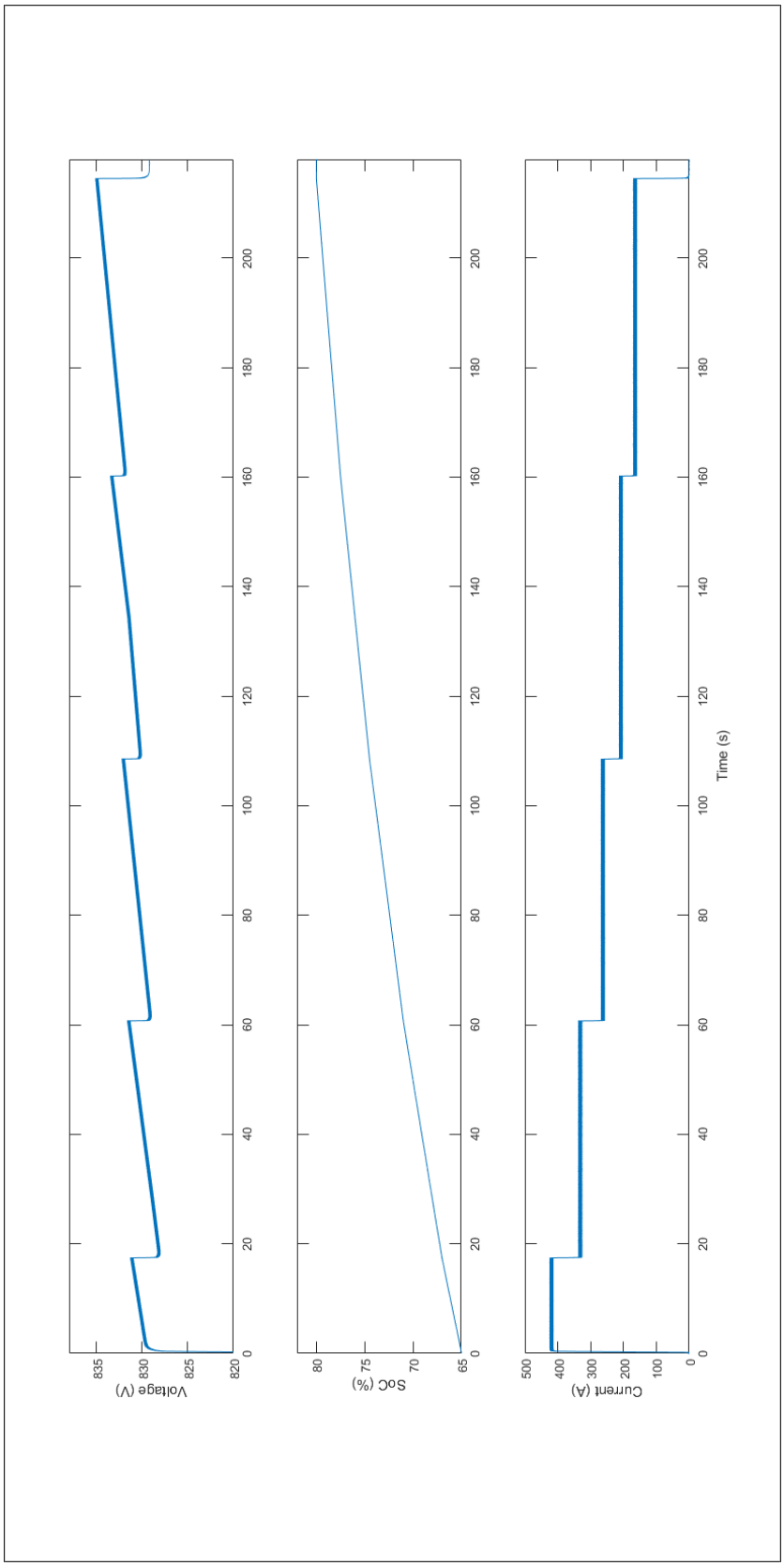

Figure 5.5: EV Battery Terminal Voltage, SoC, and Input Current During Multi-stage Constant Current Charging

5.4 PPC Efficiency

To better understand converter losses in the PPC, XML files were generated for applicable devices. Device datasheets can either be imported into the PLECS thermal library or created using the built in tool. The generated XML files can then be applied to the switching devices to account for accurate switching and conduction losses. For the IGBTs, the average power loss due to switching can be calculated by summing the pulsed energy during turn on and turn off and averaging it over the switching period. Diodes, however, do not suffer turn-on losses the same way IGBTs do and only the turn-off losses are considered. Turn-off losses in a diode are due to the reverse recovery current through the diode as it begins blocking voltage. The diodes in the PPC naturally commutate their current before shutting off, so their switching losses are not considered. Conduction losses are calculated for both by averaging the power loss due to current conduction through the on-state resistance of either the diode or the collector emitter of the IGBT. Two battery SoCs are chosen as operating points to analyze PPC losses: 20% SoC and 65% SoC. Both SoC values are operating at the first constant current stage, i_1. At 20% SoC, the PPC is operating at its lowest voltage transformation ratio. At 60% SoC, the output power is near its highest point of the charging profile and is operating with a high G_v. The converter losses for each switching device are calculated and plotted in Fig 5.6-5.9. Fig 5.6 gives the power losses for one IGBT of the active side H-bridge. Fig 5.7 shows the power losses of the IGBT in the clamp circuit. Fig 5.8 gives the conduction losses of one bridge rectifier diode and the anti-parallel clamping diode, respectively. Last, Fig 5.9 shows the total converter loss at each operating point. The total power loss can be calculated multiplied the respective losses by the number of switches in the circuit. When compared with the power output at each operating point in steady state, the converter efficiencies are calculated as 95.4% and 97.5% for 20% and 60% SoC, respectively. The 60% SoC battery charge has a 2% increase in efficiency even though the output power is higher. This is due to the reduced partial power ratio from input to output. This shows that the PPC can benefit from input voltage control.

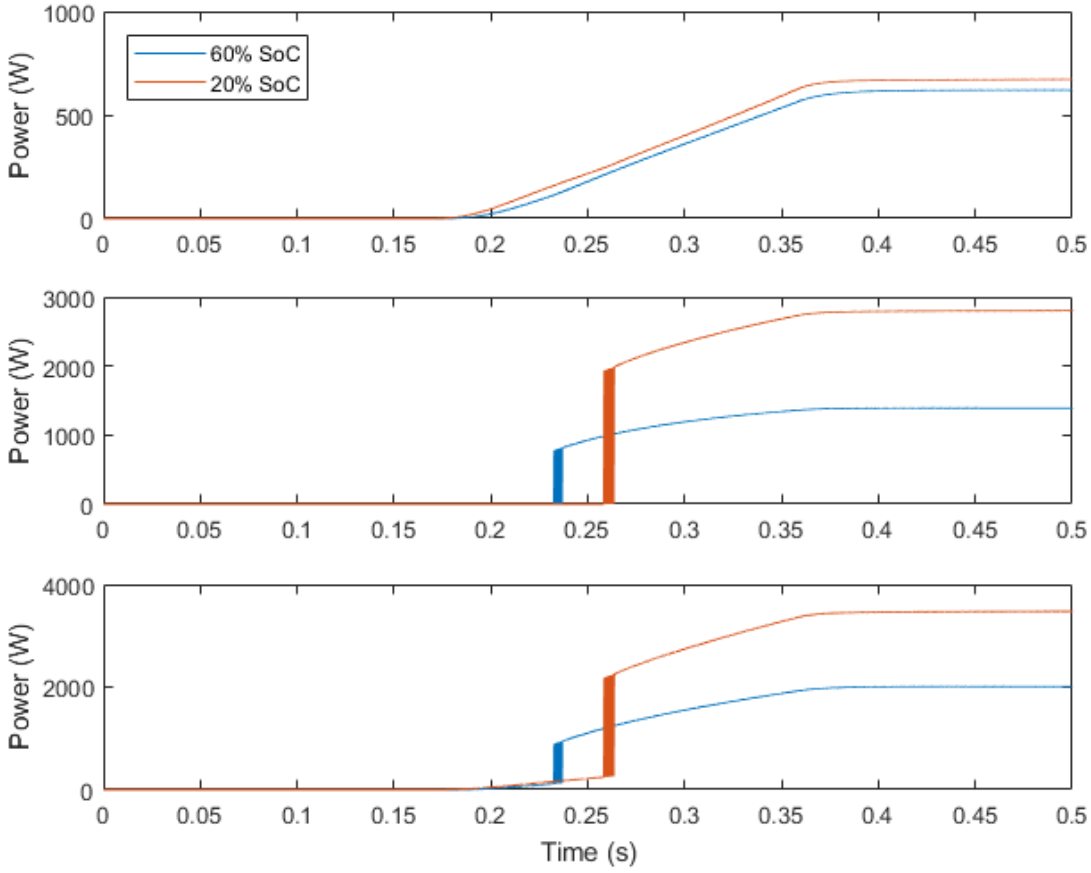

Figure 5.6: Conduction, Switching, and Total Average Power Loss in Switch A IGBT

5.5 System Operation with Multiple Vehicles

For verification at the system level, the entire station is simulated with two EV loads. The process begins by energizing the system and going through the start-up sequence previously discussed. After the MVDC bus is established, the DAB converters are enabled to ramp up the LVDC bus. Once the LVDC bus reaches the desired voltage of 1kV, the EV batteries are connected to the outputs of the PPCs. To prevent an inrush current to the clamping circuit of the PPC, a current limiting resistor is placed in series with the battery load. After a brief moment, the clamping capacitor becomes charged and begins blocking current flow to the load. At 1 s, the current limiting resistor is bypassed with a contactor and the PPCs are enabled. To demonstrate the independent operation of the PPCs, the EV batteries are initialized with different SoCs: 20% and 60%. Fig 5.11 shows

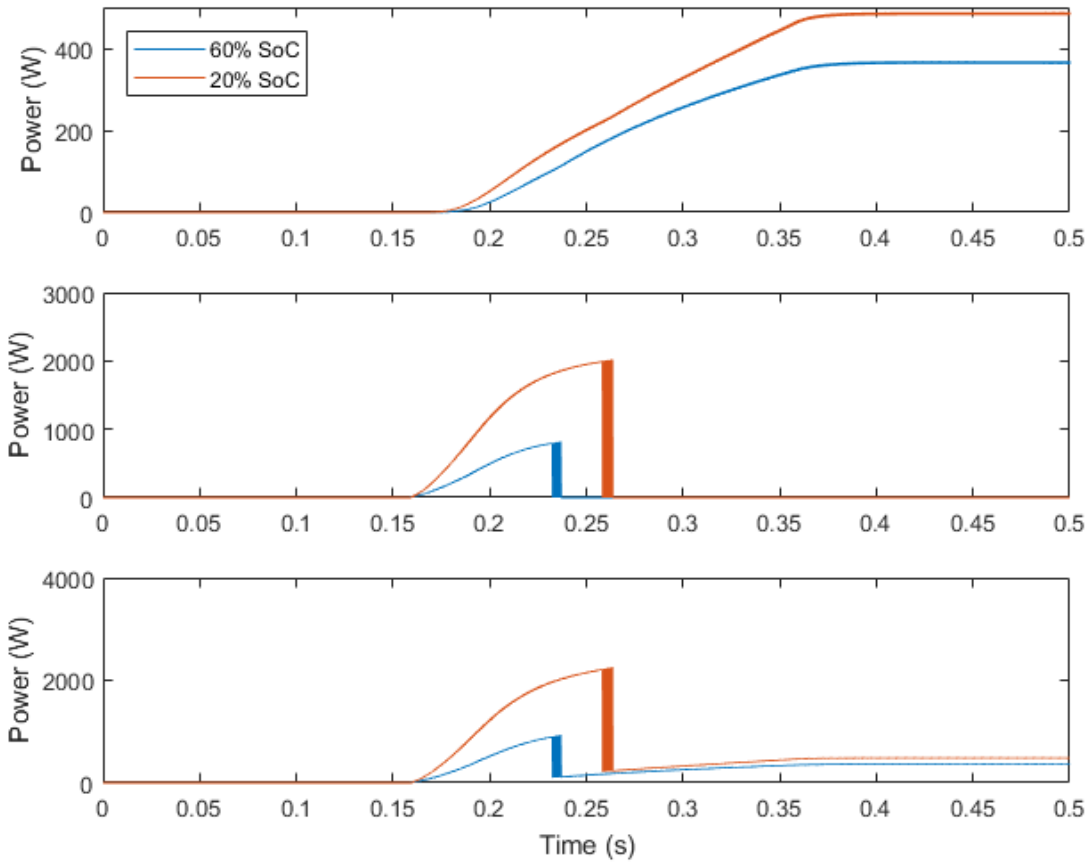

Figure 5.7: Conduction, Switching, and Total Average Power Loss in Clamping IGBT

the terminal voltage and current of each battery. Both charging currents are regulated to constant current, i_1, at their respective voltage levels. As the charging currents are ramping, an approximate 3% voltage sag can be seen on the low voltage bus in Fig 5.10. This could either be a result of the slower control response of the ISOP-DAB, or an under-sizing of DC link capacitors. This shows that the system can benefit with an energy buffer stage in the event many vehicles are connected at one time. Fig 5.12 shows the input powers from the grid interface. Analyzing the power profile over the whole operation, a few things can be seen. The system starts by successfully limiting current during the uncontrolled start up. The isolation stage forms the low voltage bus with little power draw between 0.5 and 0.75s and shows little no-load losses. Since it is able to form the LVDC bus so quickly, a possible control implementation could be to power down the DAB stage

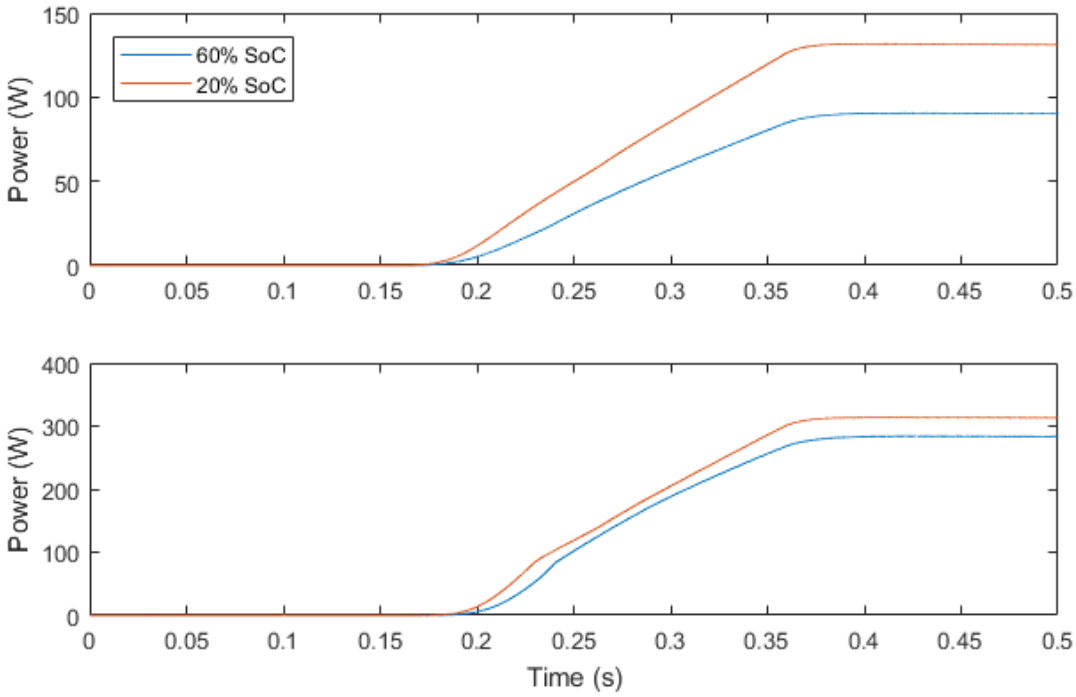

Figure 5.8: Conduction Loss in Rectifying Diode and Clamping Diode

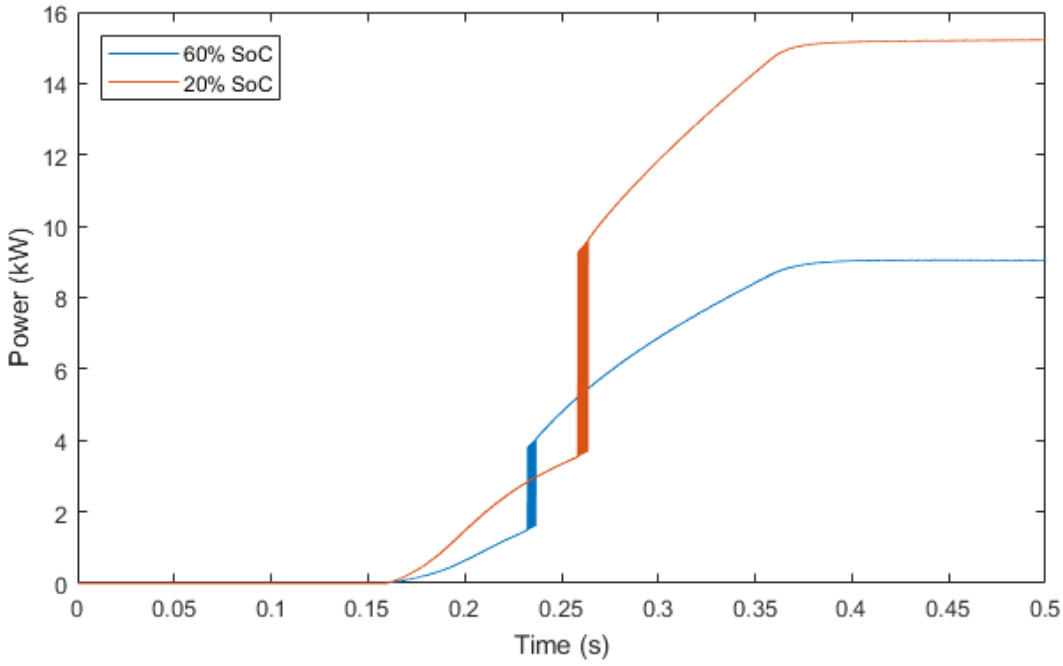

Figure 5.9: Total Average Power Loss

when no load is applied, avoiding all transformer losses. Once the PPCs reach a steady state, the system efficiency from grid to combined load is found to be 92%. It can also be seen from Fig 5.12 that after system start-up the reactive power is held to zero throughout the entire process, yielding unity power factor.

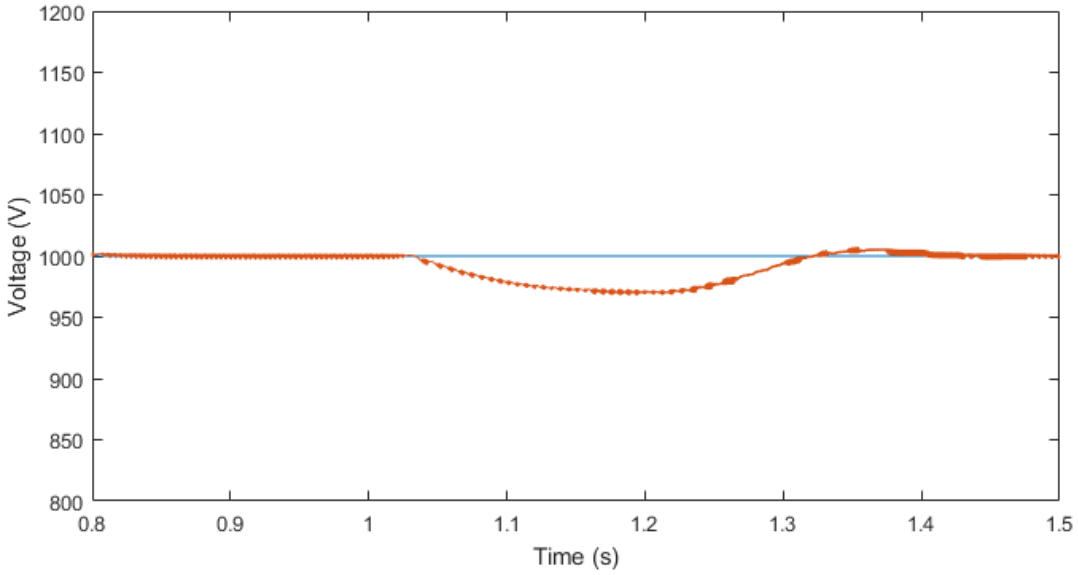

Figure 5.10: Low Voltage DC Bus Voltage During Charging

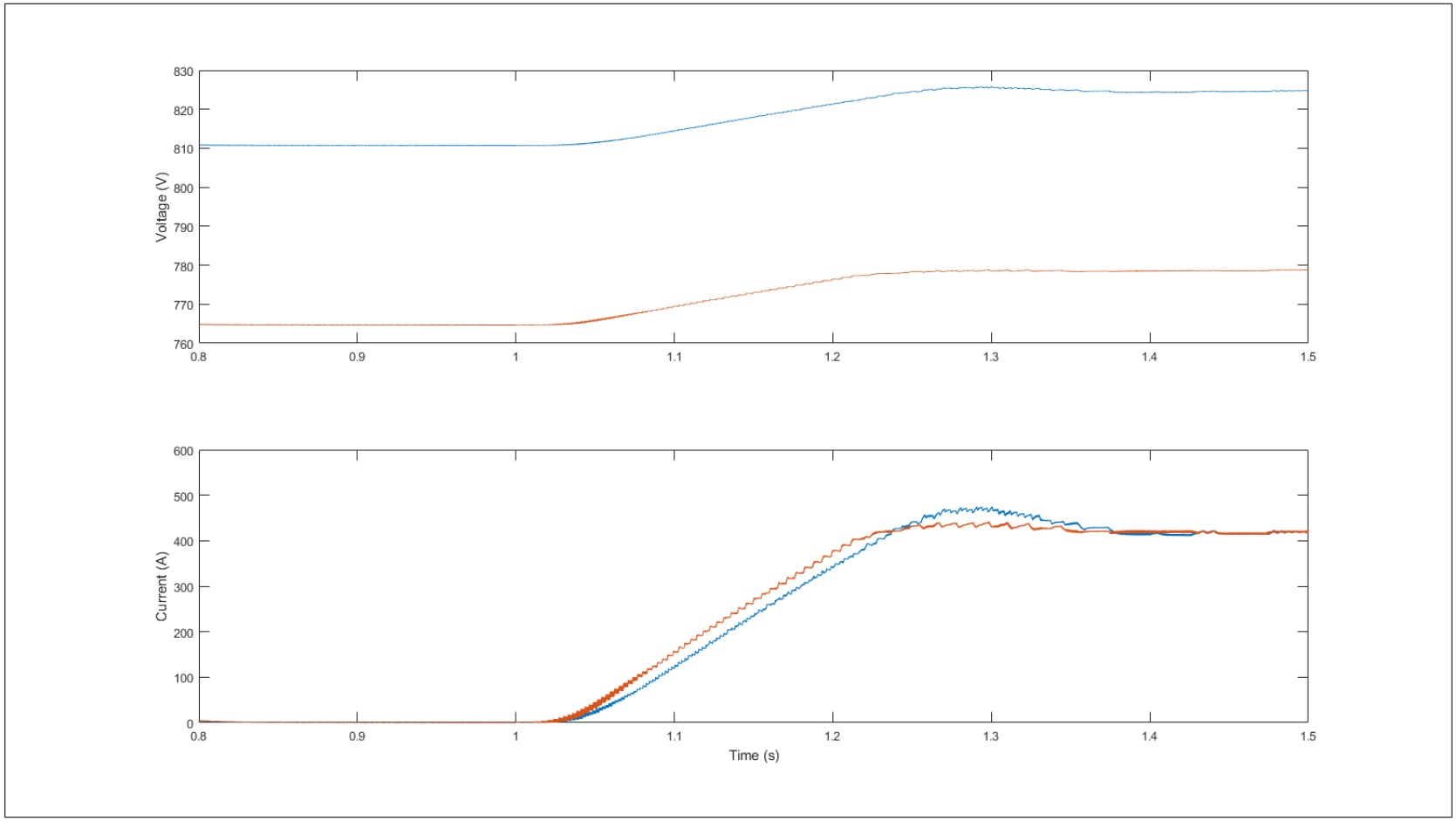

Figure 5.11: EV Battery Terminal Voltage, SoC, and Input Current During Multi-stage Constant Current Charging

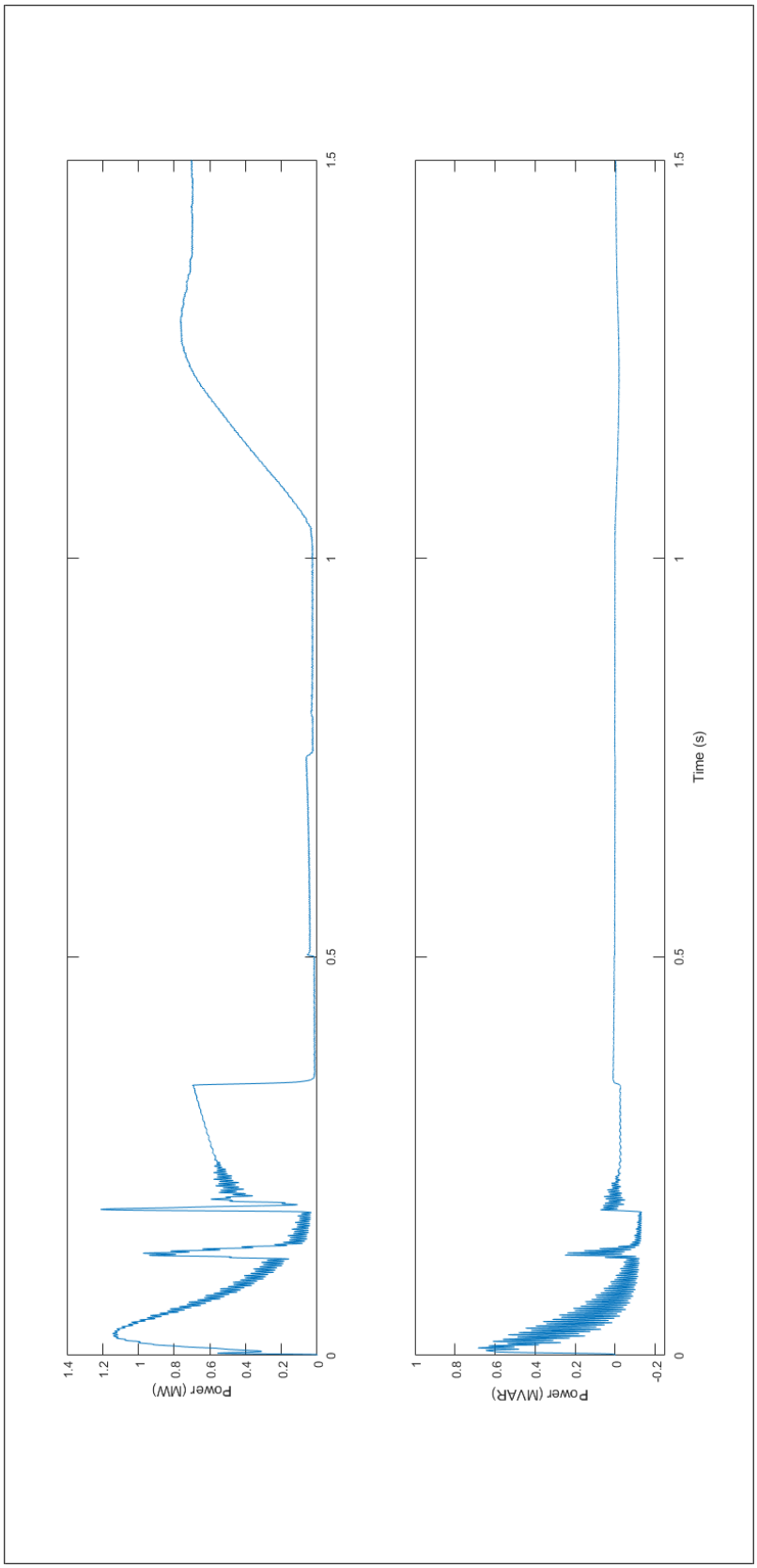

Figure 5.12: System Input Real Power and Reactive Power

CHAPTER 6
CONCLUSIONS AND FUTURE WORK

This work has presented a functional power electronic system architecture capable of servicing multiple electric vehicles at XFC levels. It utilizes a multi-level cascaded H-bridge combined with an ISOP-DAB solid state transformer to create a highly efficient, highly controllable interface with the electric grid. The partial power converter topology is given an in-depth analysis to highlight both its benefits and shortcomings. The EV battery load is considered in both its behavior and its management through SoC-based control techniques.

This architecture provides a foundation for a highly expandable system. Future work includes the implementation of a system wide control to optimize the functionality of the station. With a power electronic system, bus voltages can be adjusted to better suit the needs of a dynamic load demand. By controlling the input of the partial power converters, they can consistently operate with a low partial power ratio. This would not only extend their efficiency across an entire charge profile, but it would allow the same converter to support a wide range of battery voltages. The addition of thermal dynamics to the battery model would provide a medium to test realistic charging controls, such as pre-warming the battery prior to charging.

Further work includes the addition of battery storage. Battery storage can be used to shave peaks of short-term spikes in demand during on-peak hours. Renewable energy sources, such as solar PVs, can be added to form a micro- or nanogrid type system. With the bidirectional capability of the active front end, this is a natural transition. All such improvements would not only make an XFC station more sustainable, they would also make it very attractive to investors and future station owners.

This system also lends itself well to real-time simulation implementation. The system requires small simulation time steps to simulate switching power electronics. It also requires a long simulation run time to charge multiple EVs. With a real-time simulation platform, various multi-vehicle

controls schemes can easily be evaluated under different test scenarios. Once the system is implemented, hardware-in-the-loop testing can be conducted for controller hardware.

Finally, system protection must be considered. In a DC system, protection design can become quite complex. During a fault scenario in an AC system, the zero crossing can be taken advantage of to limit fault energy and allow the protection system to break the circuit with a relatively slow response. Faults in a DC system, however, quickly ramp up their energy with no zero crossing point. This requires a more extensive protection scheme that can identify and eliminate faulted circuits with an almost instantaneous response. To achieve this, solid state or hybrid circuit breakers with high current breaking capabilities need to be a part of the solution. With such large amounts of power delivery to each customer interface, it is imperative to have an adequate protection system.

REFERENCES

[1] EPA, "Inventory of us greenhouse gas emissions and sinks: 1990–2017," US Environmental Protection Agency, Tech. Rep., 2019.

[2] Bloomberg NEF, "Electric vehicle outlook 2019," Bloomberg Finance, Tech. Rep., 2019.

[3] D. Pevec, J. Babic, A. Carvalho, Y. Ghiassi-Farrokhfal, W. Ketter, and V. Podobnik, "Electric vehicle range anxiety: An obstacle for the personal transportation (r) evolution?" In *2019 4th International Conference on Smart and Sustainable Technologies (SpliTech)*, IEEE, 2019, pp. 1–8.

[4] L. Dickerman and J. Harrison, "A new car, a new grid," *IEEE Power and Energy Magazine*, vol. 8, no. 2, pp. 55–61, 2010.

[5] A. Burnham, E. J. Dufek, T. Stephens, J. Francfort, C. Michelbacher, R. B. Carlson, J. Zhang, R. Vijayagopal, F. Dias, M. Mohanpurkar, *et al.*, "Enabling fast charging–infrastructure and economic considerations," *Journal of Power Sources*, vol. 367, pp. 237–249, 2017.

[6] T. Bohn, *Multi-port, 1+mw charging system for medium- and heavy-duty evs: What we know and what is on the horizon?* Clean Cities Coalition Network 2020 [Webinar], https://cleancities.energy.gov/webinars26542.

[7] A. Meintz, J. Zhang, R. Vijayagopal, C. Kreutzer, S. Ahmed, I. Bloom, A. Burnham, R. B. Carlson, F. Dias, E. J. Dufek, *et al.*, "Enabling fast charging–vehicle considerations," *Journal of Power Sources*, vol. 367, pp. 216–227, 2017.

[8] D. Howell, S. Boyd, B. Cunningham, S. Gillard, L. Slezak, S. Ahmed, I. Bloom, A. Burnham, K. Hardy, A. N. Jansen, *et al.*, "Enabling fast charging: A technology gap assessment," Tech. Rep., 2017.

[9] M. Yilmaz and P. T. Krein, "Review of battery charger topologies, charging power levels, and infrastructure for plug-in electric and hybrid vehicles," *IEEE transactions on Power Electronics*, vol. 28, no. 5, pp. 2151–2169, 2012.

[10] H. Tu, H. Feng, S. Srdic, and S. Lukic, "Extreme fast charging of electric vehicles: A technology overview," *IEEE Transactions on Transportation Electrification*, 2019.

[11] Tesla, *Introducing v3 supercharging*, Tesla 2019 [Online] https://www.tesla.com/blog/introducing-v3-supercharging.

[12] C. Jung, "Power up with 800-v systems: The benefits of upgrading voltage power for battery-electric passenger vehicles," *IEEE Electrification Magazine*, vol. 5, no. 1, pp. 53–58, 2017.

[13] Porsche USA, *Porsche taycan models*, Porsche Cars North America 2020 [Online] https://www.porsche.com/usa/models/taycan/taycan-models/taycan-turbo/.

[14] Audi USA, *A thrilling future awaits: Introducing the audi e-tron gt concept*, Audi of America 2020 [Online] https://www.audiusa.com/models/audi-e-tron-gt.

[15] Ford Motor Company, *Webasto and ford team up for mustang 'lithium': Battery electric muscle car lights-up sema, signals future of performance*, Ford Media Center 2019 [Online] https://media.ford.com/content/fordmedia/fna/us/en/news/2019/11/05/webasto-ford-team-up-mustang-lithium-battery-electric-mustang-car-sema.html.

[16] General Motors, *Gm reveals new ultium batteries and a flexible global platform to rapidly grow its ev portfolio*, GM Coroporate Newsroom 2020 [Online] https://media.gm.com/media/us/en/gm/ev.detail.html/content/Pages/news/us/en/2020/mar/0304-ev.html.

[17] "Ieee standard technical specifications of a dc quick charger for use with electric vehicles," *IEEE Std 2030.1.1-2015*, pp. 1–97, 2016.

[18] S. Manzetti and F. Mariasiu, "Electric vehicle battery technologies: From present state to future systems," *Renewable and Sustainable Energy Reviews*, vol. 51, pp. 1004–1012, 2015.

[19] A. Affanni, A. Bellini, G. Franceschini, P. Guglielmi, and C. Tassoni, "Battery choice and management for new-generation electric vehicles," *IEEE Transactions on Industrial Electronics*, vol. 52, no. 5, pp. 1343–1349, 2005.

[20] C. Curry, "Lithium-ion battery costs and market: Squeezed margins seek technology improvements & new business models," *Bloomberg New Energy Finance*, 2017.

[21] J. Jaguemont, M. Abdel-Monem, N. Omar, J. van Mierlo, and P. van den Bossche, "Thermal effect of fast-charging profiles on lithium-ion batteries," in *2018 21st International Conference on Electrical Machines and Systems (ICEMS)*, IEEE, 2018, pp. 2127–2132.

[22] X.-G. Yang, T. Liu, Y. Gao, S. Ge, Y. Leng, D. Wang, and C.-Y. Wang, "Asymmetric temperature modulation for extreme fast charging of lithium-ion batteries," *Joule*, vol. 3, no. 12, pp. 3002–3019, 2019.

[23] CHAdeMO, *Chademo 3.0 released: The first publication of chaoji, the new plug harmonised with china's gb/t*, CHAdeMO Association 2020 [Online] https://www.chademo.com/chademo-3-0-released/.

[24] M. Kesler, M. C. Kisacikoglu, and L. M. Tolbert, "Vehicle-to-grid reactive power operation using plug-in electric vehicle bidirectional offboard charger," *IEEE Transactions on Industrial Electronics*, vol. 61, no. 12, pp. 6778–6784, 2014.

[25] C. Liu, K. Chau, D. Wu, and S. Gao, "Opportunities and challenges of vehicle-to-home, vehicle-to-vehicle, and vehicle-to-grid technologies," *Proceedings of the IEEE*, vol. 101, no. 11, pp. 2409–2427, 2013.

[26] K. Yunus, H. Z. De La Parra, and M. Reza, "Distribution grid impact of plug-in electric vehicles charging at fast charging stations using stochastic charging model," in *Proceedings of the 2011 14th European Conference on Power Electronics and Applications*, IEEE, 2011, pp. 1–11.

[27] J Rojas, H. Renaudineau, S. Kouro, and S. Rivera, "Partial power dc-dc converter for electric vehicle fast charging stations," in *IECON 2017-43rd Annual Conference of the IEEE Industrial Electronics Society*, IEEE, 2017, pp. 5274–5279.

[28] V. M. Iyer, S. Gulur, G. Gohil, and S. Bhattacharya, "An approach towards extreme fast charging station power delivery for electric vehicles with partial power processing," *IEEE Transactions on Industrial Electronics*, 2019.

[29] J. R. R. Zientarski, M. L. da Silva Martins, J. R. Pinheiro, and H. L. Hey, "Evaluation of power processing in series-connected partial-power converters," *IEEE Journal of Emerging and Selected Topics in Power Electronics*, vol. 7, no. 1, pp. 343–352, 2018.

[30] R. C. Cope and Y. Podrazhansky, "The art of battery charging," in *Fourteenth Annual Battery Conference on Applications and Advances. Proceedings of the Conference (Cat. No. 99TH8371)*, IEEE, 1999, pp. 233–235.

[31] A. B. Khan, V.-L. Pham, T.-T. Nguyen, and W. Choi, "Multistage constant-current charging method for li-ion batteries," in *2016 IEEE Transportation Electrification Conference and Expo, Asia-Pacific (ITEC Asia-Pacific)*, IEEE, 2016, pp. 381–385.

[32] Y.-K. Liu, K.-C. Ho, Y.-H. Liu, and S.-C. Wang, "Search for the optimal charging pattern of multi-stage constant current charging method using particle swarm optimization," in *2018 7th International Congress on Advanced Applied Informatics (IIAI-AAI)*, IEEE, 2018, pp. 536–541.

[33] X. Zhang, J. Wu, and G. Kang, "Soc estimation of lithium battery by ukf algorithm based on dynamic parameter model," in *2016 13th International Conference on Ubiquitous Robots and Ambient Intelligence (URAI)*, IEEE, 2016, pp. 945–950.

[34] M. Ye, H. Gong, R. Xiong, and H. Mu, "Research on the battery charging strategy with charging and temperature rising control awareness," *IEEE Access*, vol. 6, pp. 64 193–64 201, 2018.

[35] S. Srdic and S. Lukic, "Toward extreme fast charging: Challenges and opportunities in directly connecting to medium-voltage line," *IEEE Electrification Magazine*, vol. 7, no. 1, pp. 22–31, 2019.

[36] S. Sabri, E. Van Brunt, A. Barkley, B. Hull, M. O'Loughlin, A. Burk, S. Allen, and J. Palmour, "New generation 6.5 kv sic power mosfet," in *2017 IEEE 5th Workshop on Wide Bandgap Power Devices and Applications (WiPDA)*, IEEE, 2017, pp. 246–250.

[37] B. DeBoi, A. Lemmon, B. Nelson, C. New, and D. Hudson, "Modeling and validation of medium voltage sic power modules," in *2020 IEEE Applied Power Electronics Conference and Exposition (APEC)*, IEEE, 2020, in press.

[38] S. Du, J. Liu, J. Lin, and Y. He, "A novel dc voltage control method for statcom based on hybrid multilevel h-bridge converter," *IEEE Transactions on Power Electronics*, vol. 28, no. 1, pp. 101–111, 2012.

[39] X. Wang, J. Liu, S. Ouyang, T. Xu, F. Meng, and S. Song, "Control and experiment of an h-bridge-based three-phase three-stage modular power electronic transformer," *IEEE Transactions on Power Electronics*, vol. 31, no. 3, pp. 2002–2011, 2015.

[40] J. Zhendong, S. Yichao, W. Shuzheng, and Z. Jianfeng, "Design of a three-phase cascaded power electronic transformer based on energy internet," 2012.

[41] L. Maharjan, S. Inoue, and H. Akagi, "A transformerless energy storage system based on a cascade multilevel pwm converter with star configuration," *IEEE Transactions on Industry Applications*, vol. 44, no. 5, pp. 1621–1630, 2008.

[42] Y. Hu, J. Cheng, Y. Zhou, and G. Chen, "Control strategy of cascaded multilevel converter based on dual active bridge for wind energy conversion system," in *IECON 2017-43rd Annual Conference of the IEEE Industrial Electronics Society*, IEEE, 2017, pp. 2419–2424.

[43] D. Sha, G. Xu, and Y. Xu, "Utility direct interfaced charger/discharger employing unified voltage balance control for cascaded h-bridge units and decentralized control for cf-dab modules," *IEEE Transactions on Industrial Electronics*, vol. 64, no. 10, pp. 7831–7841, 2017.

[44] N. Yousefpoor, B. Parkhideh, A. Azidehak, S. Kim, and S. Bhattacharya, "Control and experiment of high frequency isolated modular converter under normal and ac fault operating condition," in *2014 IEEE Energy Conversion Congress and Exposition (ECCE)*, IEEE, 2014, pp. 5813–5820.

[45] Y. Liu, A. Q. Huang, W. Song, S. Bhattacharya, and G. Tan, "Small-signal model-based control strategy for balancing individual dc capacitor voltages in cascade multilevel inverter-based statcom," *IEEE Transactions on Industrial Electronics*, vol. 56, no. 6, pp. 2259–2269, 2009.

[46] H. Akagi, "Classification, terminology, and application of the modular multilevel cascade converter (mmcc)," *IEEE Transactions on power electronics*, vol. 26, no. 11, pp. 3119–3130, 2011.

[47] Y. Li, Y. Wang, and B. Q. Li, "Generalized theory of phase-shifted carrier pwm for cascaded h-bridge converters and modular multilevel converters," *IEEE Journal of Emerging and Selected Topics in Power Electronics*, vol. 4, no. 2, pp. 589–605, 2015.